https://doi.org/10.5194/egusphere-2026-3008
Preprint. Discussion started: 2 July 2026

Multi-scenario Hydro-climatic Mean and Peak Responses of Central–South Asia and the Tibetan Plateau to Future Warming and Stratospheric Aerosol Intervention

Azfar Hussain [1,2,3], Huizeng Liu [2,3,*], Abolfazl Rezaei [4], Ping Zhu [2], Daniele Visioni [5], Guanglang Xu [2], Chao Yang [3], Yan Ma [2], Tianye Cao [2], Qingquan Li[2,3]

[1] College of Civil and Transportation Engineering, Shenzhen University, Shenzhen 518060, China

[2] Institute for Advanced Study & Tiandu-Shenzhen University Deep Space Exploration Joint Laboratory & Space Science Center, Shenzhen University, Shenzhen 518060, China

[3] MNR Key Laboratory for Geo-Environmental Monitoring of Great Bay Area & Guangdong Key Laboratory of Urban Informatics & Shenzhen Key Laboratory of Spatial Smart Sensing and Services, Shenzhen University, Shenzhen 518060, China

[4] Department of Earth Sciences, Institute for Advanced Studies in Basic Sciences, Zanjan 45137–66731, Iran

[5] Department of Earth and Atmospheric Sciences, Cornell University, Ithaca, NY, USA

[*] Corresponding author, E-mail: huizeng.liu@szu.edu.cn

https://doi.org/10.5194/egusphere-2026-3008
Preprint. Discussion started: 2 July 2026

ABSTRACT

Central–South Asia and the Tibetan Plateau are climate-sensitive regions where water resources are controlled by monsoon, westerlies, and cryosphere processes. This study evaluates hydroclimatic changes across three regimes: moisture-limited Central Asia (west (WCA) and east (ECA)), cryosphere-influenced Tibetan Plateau (TIB), and monsoon-dominated South Asia (SAS), under warming (SSP2-4.5, SSP5-8.5) and solar radiation management (SRM) scenarios with temperature-stabilized (G6-1.5K-SAI and Geo-SAI) and transient forcing (G6solar and G6sulfur) experiments using CESM2-WACCM for 2055–2084 relative to 2015–2034. Warming substantially amplifies annual peak hydroclimatic responses, with peak temperature increasing by 24%, ET by 6.5%, precipitation by up to 13% in TIB and SAS, and available water (AW) by 18%–23%, alongside accelerated cryosphere melts and enhanced vegetation. In contrast, dry Central Asia shows smaller precipitation and AW increases but remains highly sensitive to evapotranspiration (ET)-driven drying and soil moisture (SM) losses. Temperature-stabilized scenarios provide stronger and more consistent suppression of warming and extremes, while transient forcing scenarios achieve only partial mitigation and retain greater variability. Across regions, SRM generally reduces temperature and ET, produces mixed precipitation responses, and partially restores AW, soil moisture, and cryosphere-related processes. The findings per unit sulfur injected exhibit highest cooling and hydrological efficiency under G6-1.5K-SAI, showing that effectiveness depends on both sulfur loading and injection strategy. SRM also moderates cryosphere loss through enhanced snowfall and reduced snowmelt over the TIB. Warming intensifies seasonal variability and advances peak timing, whereas SRM dampens these shifts to present-day conditions. Precipitation remains the dominant control on AW, indicating that SRM primarily modifies hydroclimatic magnitude rather than underlying water-cycle controls. Overall, SRM reduces hydroclimatic extremes but cannot fully offset regional water stress, and its effectiveness depends on both forcing pathway and intervention strategy, highlighting the need for climate-regime-specific and sulfur-normalized evaluation.

Keywords: Solar geoengineering impacts, Hydroclimatic variability, Land–atmosphere interactions, Available water resources, Climate mitigation

https://doi.org/10.5194/egusphere-2026-3008
Preprint. Discussion started: 2 July 2026

1. Introduction

Central and South Asia, encompassing West-Central Asia (WCA), East-Central Asia (ECA), the Tibetan Plateau (TIB), and South Asia (SAS), is among the most climate-sensitive regions globally. The region is already experiencing increasing climate stress, including frequent droughts (Jiang and Zhou, 2023) and growing water scarcity (Wu et al., 2025). The WCA and SAS is among the world's most densely populated and rapidly developing regions (Ullah et al., 2022; Voumik et al., 2023), where hundreds of millions of people depend directly on climate-sensitive water resources for agriculture, hydropower, and domestic use (Hermans et al., 2025; Zhu et al., 2024; Akram et al., 2024). Accelerated glacier retreat, ice thinning, and permafrost thaw are driving rapid changes in the Asian Water Tower on the TIB, raising concerns for the long-term sustainability of freshwater resources serving nearly two billion people (Wang et al., 2025). Regional hydroclimate is shaped by the interaction of the South Asian monsoon (Hussain et al., 2024b), mid-latitude westerlies (Cheng et al., 2025), and cryosphere processes over the TIB (Wang et al., 2025), which together regulate precipitation, snow accumulation, glacier melt, and downstream runoff. Ongoing warming has already altered monsoon dynamics and intensified hydroclimatic extremes, with rising evaporative demand, shifting precipitation patterns, and declining soil moisture (SM) contributing to more frequent and severe droughts and floods (Haile et al., 2020; Kim and Bae, 2020; Samaniego et al., 2018; Stevenson et al., 2022). These coupled atmospheric and cryosphere sensitivities make the region particularly vulnerable to changes in temperature and precipitation, amplifying risks to water security, agriculture, ecosystems, and livelihoods. Consequently, understanding how distinct SRM strategies modulate temperature, precipitation, cryosphere processes, and land–atmosphere interactions is critical for assessing their implications for future water resources.

The TIB remains highly sensitive to climate change because it plays a central role in shaping atmospheric circulation and sustaining regional freshwater resources (Li et al., 2022b; Lin et al., 2023). Previous observations indicate that terrestrial water storage across the TIB decreased by approximately 10.2 Gt per year during 2002–2017 (Li et al., 2022b). Meanwhile, future projections suggest that continued high-emission conditions may promote lake expansion and modify precipitation regimes in the region (Chen et al., 2022; Zhu et al., 2025). Under the SSP5-8.5 scenario, warming could reach as much as 4.8°C by the end of the century (Effiong and Neitzel, 2016), potentially amplifying hydroclimatic extremes such as droughts and floods, while also altering soil moisture, evapotranspiration, and runoff dynamics (Samaniego et al., 2018; Vicente-Serrano et al., 2020). Under SSP5-8.5, this warming is expected to alter water fluxes, thereby reshaping runoff patterns, disrupting the water cycle, and affecting overall water availability (Price et al., 2022). Simultaneously, shifts in monsoon behavior indicate a growing trend toward aridity,

https://doi.org/10.5194/egusphere-2026-3008
Preprint. Discussion started: 2 July 2026

placing even greater pressure on already stressed water resources (Simpkins, 2020). This increasing aridity is expected to significantly elevate the frequency of severe drought episodes (Park et al., 2018).

Global warming is disrupting water availability (Vicente-Serrano et al., 2020), for agriculture and livelihoods (Naumann et al., 2018) in Central Asia. Projections indicate hydroclimatic shifts (Ma et al., 2021), drying SM and runoff in the WCA, while increased wetting in east, and widespread rise in drought frequency (Hua et al., 2022). Global warming produces a robust increase over the Tianshan Mountains and northern regions, despite differences in emission trajectories (Jiang et al., 2020). Despite this projected increase, water availability in Central Asia remains under serious threat, as the terrestrial water is declining, primarily due to anthropogenic changes to surface water areas (Huang et al., 2021). Similar climate-related pressures are also evident across Central Asia, where changes in monsoon behavior, together with rising temperatures and glacier retreat in the Tianshan–Pamir ranges, are increasing the region's vulnerability to water scarcity (Huang et al., 2021; Fallah et al., 2024; Yu et al., 2021).

Solar radiation modification (SRM), often described as solar geoengineering, has received growing attention as a potential supplementary approach for limiting the impacts of anthropogenic greenhouse gas (GHG)–driven warming (Rezaei et al., 2025a; Richter et al., 2022). Stratospheric aerosol injection (SAI), a prominent SRM technique, is a potential climate intervention strategy that aims to partially offset GHG–driven global warming (Crutzen, 2006; Irvine and Keith, 2020; Ricke et al., 2023; Tilmes et al., 2018). By introducing reflective aerosols into the stratosphere, SAI is designed to increase planetary albedo and reduce incoming shortwave radiation, thereby mimicking the transient cooling effects observed after major volcanic eruptions (Pope et al., 2012; Weisenstein et al., 2015). However, while SAI has the potential to moderate global temperature rise, its broader hydroclimatic consequences remain uncertain, particularly for precipitation, runoff, and aridity (Rezaei et al., 2025b). These uncertainties raise concerns that SAI could intensify water stress in monsoon-dominated and arid regions (Robock et al., 2008; Niemeier and Schmidt, 2017; Cheng et al., 2019; Liu et al., 2024; Simpson et al., 2019; Macmartin et al., 2017). Previous studies indicate that SAI may dampen the hydrological cycle by suppressing precipitation and modifying runoff processes through changes in land–atmosphere interactions, vegetation responses, and snowmelt-related fluxes (Robock et al., 2008; Niemeier and Schmidt, 2017; Cheng et al., 2019; Liu et al., 2024; Simpson et al., 2019; Macmartin et al., 2017). Such impacts are particularly important across Asia, where complex topography and monsoon circulation produce strong hydroclimatic

https://doi.org/10.5194/egusphere-2026-3008
Preprint. Discussion started: 2 July 2026

gradients, while year-to-year variability is further influenced by spring snow cover, soil moisture, and ENSO-driven sea surface temperature anomalies (Zhu et al., 2023; Wang et al., 2008).

Coordinated SRM experiments such as G6-1.5K-SAI, G6solar, G6sulfur, and Geo-SAI have been designed to assess the extent to which SRM could partially offset warming under various emissions pathways (Agada et al., 2025; Visioni et al., 2020b; Visioni et al., 2024; Bonou et al., 2023; Moore et al., 2024). Recent Geoengineering Model Intercomparison Project (GeoMIP) and G6-1.5K-SAI experiments include both aerosol-based SRM (e.g., G6sulfur, G6-1.5K-SAI, and Geo-SAI) and idealized solar dimming (e.g., G6solar), enabling isolation of radiative effects from aerosol processes. Together, these scenarios provide a framework to assess how different SRM strategies operate under distinct experimental designs and emissions pathways. In particular, G6-1.5K-SAI and Geo-SAI aim to reduce global temperatures at approximately 1.5 °C under SSP2-4.5 and SSP5-8.5, respectively, whereas G6solar and G6sulfur are designed to offset the additional radiative forcing of SSP5-8.5 relative to SSP2-4.5 (Kravitz et al., 2013b; Simpson et al., 2019; Visioni et al., 2020). For instance, the Geo SSP5-8.5 1.5 experiment, hereafter referred to as Geo-SAI, is designed to limit global temperature increase to approximately 1.5°C while still following an SSP5-8.5 emissions trajectory (Tilmes et al., 2020). Although research on SAI has expanded considerably, important knowledge gaps remain regarding its region-specific effects on hydrological processes across Asia. Existing studies have mainly emphasized global-scale or zonal changes in precipitation (Kravitz et al., 2013a; Bala et al., 2008; Huynh and Mcneill, 2024; Schiferl et al., 2018), whereas comparatively limited attention has been given to vegetation dynamics and terrestrial water storage responses, both of which play critical roles in regulating hydroclimatic extremes (Clark et al., 2023; Schiferl et al., 2018).

This study addresses these gaps by analyzing future changes in mean, peak, and seasonal amplitude values as well as the timing of annual peak of nine hydroclimatic variables across WCA, ECA, TIB and SAS under GHG-emissions without (SSP2-4.5 and SSP5-8.5) and with SRM (G6-1.5K-SAI, G6solar, G6sulfur, and Geo-SAI). For interpretation, we classify the experiments into temperature-stabilized scenarios (G6-1.5K-SAI and Geo-SAI) and transient forcing scenarios (G6solar, and G6sulfur). We then evaluate their impacts on available water (AW) resources. Using outputs from the CESM2 model, we assess changes in nine key variables—temperature, precipitation, ET, AW, snowfall flux, snowmelt flux, surface runoff, SM, and leaf area index (LAI)—with an emphasis on spatial heterogeneity, extreme event modulation and impacts on water resources. The aim is to evaluate whether SRM could moderate GHG-emissions-induced changes in hydroclimatic characteristics of and influence on water resources or instead introduce new challenges in the

https://doi.org/10.5194/egusphere-2026-3008
Preprint. Discussion started: 2 July 2026

regions. This regional focus advances global-scale analyses by revealing how SRM's effects on hydroclimatic variables differ across the contrasting environments, providing deeper insight into its potential benefits and risks for regional freshwater sustainability. Additionally, to assess whether the drivers of AW change in future climates, we used separate multiple linear regression (MLR) models in each specific region under all scenarios.

2. Data and methods

2.1. Study area

The study region spans approximately from 8° to 45° N latitude and 40° to 100° E longitude (**Figure 1**), Geographically stretching from the Caspian Sea in the west to the Xinjiang Uygur Autonomous Region in the northeast, the TIB in the east, and the Indo-Gangetic Plain and peninsular India in the south, extending toward the Indian Ocean. The spatial distribution of precipitation across this region shows pronounced regional contrasts, largely shaped by monsoon influence, westerlies, and topography during 2000–2024 as observed from ERA5 datasets. The WCA and ECA are drier regions in comparison to cold-TIB and warm-SAS (Iturbide et al., 2020).

Central Asia lies within the dominant influence zone of the mid-latitude westerly circulation, which plays a primary role in controlling regional precipitation variability (Wei et al., 2023). Consequently, precipitation is largely concentrated in winter and spring due to the combined influence of the westerly jet stream and the North Atlantic Oscillation (Zhang et al., 2019; Yang et al., 2020). The western and northwestern plains of Central Asia receive moisture from Atlantic westerlies and cold northerly inflows, while the Himalayas–Tibetan Plateau–Pamir system limits moisture transport from the Indian Ocean (Zhang et al., 2019; Schiemann et al., 2008; Bothe et al., 2012; Zou et al., 2021). The TIB lies in a transition zone between mid-latitude westerlies and the Asian monsoon system, leading to strong seasonal precipitation variability, with summer monsoon rainfall dominating and winter precipitation linked to westerly disturbances (Hussain et al., 2021; Wang et al., 2025; Botsyun et al., 2022). Summer precipitation is the main source of land surface water over the Tibetan Plateau, with more than 60% of annual precipitation occurring during the wet season (Dong et al., 2024), whereas the westerlies dominate the winter precipitation (Wang et al., 2023a). The South Asian Summer Monsoon brings abundant precipitation to SAS, providing a major water resource and sustaining billions of people in the region (Luo et al., 2024). During boreal summer, the Intertropical Convergence Zone shifts northward over SAS, enhancing moisture convergence and deep convection that drive the SAS monsoon. While land–sea thermal contrast and orography shape regional rainfall, remote forcings also play an important role. For example, high-latitude insolation changes influence long-term monsoon variability (Zhang et al.,

https://doi.org/10.5194/egusphere-2026-3008
Preprint. Discussion started: 2 July 2026

2023), and extratropical cloud feedbacks and Southern Ocean heat uptake can strengthen monsoon circulation and rainfall under warming (Chen et al., 2024).

The TIB exhibits moderate precipitation ranging from 500–1500 mm/year, with higher amounts in the southern and southeastern margins due to monsoonal uplift, while the north and west remain relatively dry. In contrast, SAS receives the greatest rainfall, exceeding 1500 mm/year and peaking around 2500 mm/year in the monsoon-dominated core, making it the wettest subregion (**Figure 1**).

The WCA includes countries such as eastern Turkey, Georgia, Armenia, Azerbaijan, Iraq, Iran, Afghanistan, Kyrgyzstan, Kazakhstan, Tajikistan, Uzbekistan, and Turkmenistan. The ECA covers northwestern China, particularly the Xinjiang Uygur Autonomous Region, and includes geographical features such as the Kunlun Mountains, Taklamakan Desert, Gobi Desert, and southern Mongolia. The TIB bounds southern border of ECA, while SAS lies to the south of both WCA and the TIB, encompassing southern Pakistan, India, Bangladesh, and Myanmar. The greater Himalayas form a natural climatic and geographical divide between the TIB and SAS. The TIB is highly sensitive and vulnerable to climate change influencing the water resources and the ecosystem (Luo et al., 2024; Hu et al., 2024), whereas atypical heating over the TIB increased the compound SAS heatwave extremes and related atmospheric anomalies (Jin et al., 2024). Collectively, the subregions have very distinct climates and extreme conditions indicating a climate-sensitive region, which is highly vulnerable to the impacts of global warming.

2.2 Model simulations and scenarios

In this study, we use the Community Earth System Model version 2 with the Whole Atmosphere Community Climate Model version 6 (CESM2–WACCM6), developed by the National Center for Atmospheric Research (NCAR) (Eyring et al., 2016; Rezaei et al., 2024, 2023; Tilmes et al., 2020), to simulate hydroclimatic responses under moderate (SSP2–4.5) and high (SSP5–8.5) GHG-emissions baseline scenarios for G6-1.5K-SAI, G6solar, G6sulfur, and Geo-SAI in present-day conditions (2015–2034) and future (2055–2084) periods. Here, SSP2–4.5 is used as the baseline scenario for G6-1.5K-SAI, whereas SSP5–8.5 is used as the baseline for G6solar, G6sulfur, and Geo-SAI.

CESM2-WACCM6 is a fully coupled Earth system model with interactive representations of the atmosphere, ocean, land, and sea ice, allowing it to simulate global-scale climate variability and long-term climate change (Gettelman et al., 2019). Evaluations comparing CESM2 with CESM1 show that CESM2 performs strongly across multiple assessment metrics and is often ranked among the better-performing models (Simpson et al., 2020; Magara et al., 2025). The model has also

https://doi.org/10.5194/egusphere-2026-3008
Preprint. Discussion started: 2 July 2026

shown improved capability in representing precipitation over dry regions, including Central Asia (Guo et al., 2021), Africa (Mmame et al., 2023), and the Middle East and North Africa (Rezaei et al., 2024). Under the SSP5-8.5 high-emissions pathway, CESM2 simulates approximately 1°C greater warming than CESM1, whereas both models produce broadly similar temperature projections by 2100 under the lower-emission SSP2-4.5 and SSP1-2.6 scenarios (Duffey and Irvine, 2024; Clark et al., 2023). CESM2-WACCM also incorporates a detailed vertical configuration with 70 atmospheric levels (Keeble et al., 2020), spanning from the surface pressure level of 1000 hPa to 4.5×10^{-6} hPa, which extends into the lower thermosphere at nearly 140 km altitude (Meehl et al., 2020). Its horizontal grid spacing of 0.9° latitude × 1.25° longitude, equivalent to roughly 100 km × 140 km near the equator, further supports the representation of regional climate characteristics and atmosphere–surface interactions (Liang et al., 2022).

G6-1.5K-SAI simulates stratospheric aerosol injection (SAI) to maintain global warming at approximately 1.5 °C above preindustrial levels in each model and incorporates several design updates relative to the earlier GeoMIP G6sulfur experiment (Visioni et al., 2024). The experiment injects SO_2 at two subtropical latitudes and uses a more realistic middle-of-the-road emissions scenario and start date than earlier studies (Bednarz et al., 2026). This experiment use an intermediate emissions baseline (SSP2-4.5), a delayed deployment start date reflecting both the anticipated exceedance of 1.5 °C warming and plausible implementation timelines, and an injection strategy that avoids the tropical pipe—featuring injections at 30°N and 30°S rather than near-equatorial locations—to achieve a more latitudinally uniform aerosol distribution (Visioni et al., 2024). In contrast, the G6solar, G6sulfur, and Geo-SAI scenarios are implemented relative to a SSP5–8.5 baseline, representing a high-emissions, fossil-fueled development pathway. These experiments are designed to assess the ability of different SRM strategies to counteract strong GHG–driven warming under a high forcing background (Visioni et al., 2021; Visioni et al., 2024; Visioni et al., 2022; Jones et al., 2021; Feng et al., 2025; Fernández et al., 2024).

The G6solar experiment, conducted under the GeoMIP framework (Kravitz et al., 2011), represents an idealized SRM scenario. It aims to reduce warming under SSP5-8.5 to levels similar to SSP2-4.5 (Visioni et al., 2021), just like the G6sulfur counterpart. G6solar uses idealized solar dimming to achieve global-mean cooling (Gay et al., 2025), thereby mimicking the radiative effects of a space sunshade without explicitly simulating SAI (Tan et al., 2024), with the similar protocol as G6sulfur. As a result, G6solar serves as a useful benchmark for distinguishing hydroclimatic responses driven purely by radiative forcing from those associated with aerosol-induced stratospheric heating, circulation changes, and cloud–radiation interactions.

https://doi.org/10.5194/egusphere-2026-3008
Preprint. Discussion started: 2 July 2026

The G6sulfur experiment modifies the high-forcing SSP5–8.5 scenario (O'neill et al., 2016), to follow the temperature evolution of the medium-forcing SSP2–4.5 pathway over 2020–2100 by introducing gradually increasing amounts of stratospheric sulfate aerosol injection, providing a physically explicit representation of SAI under high-emissions conditions (Jones et al., 2022). In this scenario, sulfur dioxide is injected into the tropical lower stratosphere, where it oxidizes to form sulfate aerosols that increase planetary albedo and reflect a portion of incoming solar radiation back to space (Rezaei et al., 2025a). In CESM2–WACCM6, SO_2 is injected at approximately 25 km altitude, and the injection rate is adjusted annually to achieve a prescribed radiative forcing target, with aerosol loading increasing over time to offset the rising GHG–induced warming (Rezaei et al., 2025a; Danabasoglu, 2023).

The Geo-SAI experiment aims to stabilize global mean temperatures at 1.5 °C (Jones et al., 2022; Tilmes et al., 2020) above pre-industrial levels (1850–1900) under SSP5-8.5 greenhouse gas emissions. Climate models suggest it could reduce global (Richter et al., 2022), and Arctic temperatures while enhancing Northern Hemisphere Sea ice coverage (Wheeler et al., 2025), and similarly restore southern hemisphere cyclone activity (Reboita et al., 2025; Reboita et al., 2024). Geo-SAI implements SO_2 injections at 30°N, 15°N, 15°S, and 30°S, with injection rates governed by a feedback control algorithm designed to simultaneously regulate global mean temperature, interhemispheric temperature contrast, and pole-to-equator gradients (Tilmes et al., 2020). Geo-SAI predominantly concentrates SO_2 injections at 30°N and 30°S, with smaller contributions at 15°N and minimal injection elsewhere, and by the end of the 21st century the total injection rate increases to approximately 48 Tg SO_2 yr^{-1} (Tilmes et al., 2020).

Importantly, these experiments differ not only in their emissions background but also in their control objectives, injection strategies, and total sulfur burden. In particular, G6sulfur injects sulfur across a broad equatorial band (10°N–10°S), whereas Geo-SAI uses four discrete latitudes (15°N, 15°S, 30°N, 30°S) and G6-1.5K uses only two discrete latitudes (30°N, 30°S) (Visioni et al., 2024; Lee et al., 2025; Bednarz et al., 2026; Rezaei et al., 2025a) (**Table S2**). Injection rates and total sulfur burdens vary across experiments and evolve over time in response to their respective control objectives, with generally larger interventions required under high-emissions scenarios (Visioni et al., 2024; Tilmes et al., 2020). Differences in injection latitude (tropical versus subtropical) further influence aerosol distribution, radiative forcing, and large-scale circulation responses (Visioni et al., 2020a; Tilmes et al., 2018). As a result, inter-experiment differences in hydroclimatic responses reflect both the magnitude and design of the interventions, and should not be interpreted solely as differences in effectiveness. For example, Geo-SAI reaches injection rates of up to ~48 Tg SO_2 yr^{-1}

https://doi.org/10.5194/egusphere-2026-3008
Preprint. Discussion started: 2 July 2026

(Rezaei et al., 2025a), as it is trying to offset over 5C of warming by the end of the century, whereas injection magnitudes in G6-1.5K-SAI and G6sulfur are generally lower as they are trying to offset between 2 and 3C of warming. and the location of injection for Geo-SAI varies dynamically depending on the control objective. These differences in sulfur burden highlight that the strength of the intervention differs substantially across experiments.

To facilitate comparison across experiments, the key characteristics of SAI in these experiments, including injection strategy, location, altitude, and mean injection rates are summarized in **Table S2**. The reported values represent mean SO_2 injection rates during 2055–2084, while recognizing that injection magnitudes may vary over time under feedback-controlled designs. These differences in sulfur burden and deployment strategy are explicitly accounted for in this study through normalization of hydroclimatic responses by sulfur injection, enabling a consistent assessment of intervention efficiency across temperature-stabilized and transient forcing experiments.

We used monthly data for temperature, precipitation, ET, AW (precipitation minus actual ET), snowfall flux, snowmelt flux, runoff, SM, LAI (**Table S1**), from all available ensemble members of the scenario. For the analysis, we used the ensemble mean of the SSP2-4.5 and SSP5-8.5 data over 2015-2034 as a baseline (present-day conditions). The 2055–2084 were selected as future period for all GHG-emission and SRM scenarios to be compared with present-day conditions.

2.3 Mann-Kendall test and Sen's slope estimator

The spatiotemporal significant trends in hydroclimatic variables under each scenario are assessed through the nonparametric Mann-Kendall test (Kendall, 1955; Mann, 1945) that makes no distributional assumption and is resistant to outliers. The null hypothesis states that there is no trend (Hussain et al., 2025b; Hussain et al., 2024c). Statistical significance is assessed with the standardized test statistic *Z*; a trend is deemed significant at the 5% level (Ullah et al., 2023c). The Sen's slope estimator (Sen, 1968) is used to assess the magnitude of the trend in the hydroclimatic factors (Rebi et al., 2023; Nawaz et al., 2023). The positive (negative) value shows increasing (decreasing) trends (Guan et al., 2017; Guan et al., 2015).

2.4 Changes and shifts in seasonal dynamics

We evaluated changes in seasonal amplitude and peak timing for nine land-surface variables, namely temperature, precipitation, ET, AW, snowfall flux, snowmelt flux, runoff, SM, and LAI, under each scenario for 2055–2084 relative to the baseline period of 2015–2034. Seasonal cycles were examined using ensemble-mean monthly anomalies, from which the month of annual maximum occurrence and the associated amplitude changes were determined. Following the

https://doi.org/10.5194/egusphere-2026-3008
Preprint. Discussion started: 2 July 2026

harmonic regression approach of Rezaei et al. (2025a), shifts in seasonal behavior were quantified for each variable and subregion. Specifically, the annual peak timing (P) and seasonal amplitude (Amp) were estimated to characterize both the strength of intra-annual variability and the timing of maximum seasonal expression. These metrics were then compared between the historical baseline and future climate scenarios to assess changes in the magnitude and timing of seasonality. Statistically significant differences from the baseline period were determined using two-sided t-tests at the $P < 0.05$ level.

2.5 Multiple linear regression (MLR) framework

We used MLR to predict AW variability based on the regional hydro-climatic variables (i.e., temperature, precipitation, ET, snowfall flux, snowmelt flux, runoff, SM, and LAI) to determine whether the hierarchy of variable importance would change under SRM experiments (G6-1.5K-SAI, G6solar, G6sulfur and Geo-SAI) relative to their corresponding GHG-emissions baselines (SSP2-4.5 and SSP5-8.5). For each region (WCA, ECA, TIB, and SAS) and scenario, we fit separate MLR models following a fixed pipeline: (i) screening for multicollinearity with correlation-based variable clustering and variance inflation factors (VIF), (ii) outlier detection and removal, (iii) inspection of temporal autocorrelation and construction of lagged predictors, (iv) refitting a final model with the selected lagged terms, and (v) decomposing the model R^2 into relative importance with LMG; (Lindeman et al., 1980) contributions for interpretation. The general MLR is expressed through Equation (1) as:

$$Y_t = \beta_0 + \sum_{k=1}^{p} \beta_k X_{k,t} + \sum_{k=1}^{p} \sum_{l \in L_k} \gamma k, l X_{k,t-l+\varepsilon t,} \quad (1)$$

where Y_t is AW, $X_{k,t}$ are predictors, $X_{k,t-l}$ are selected lags with $l \in L_k$, and εt is the error term.

Relative importance of predictors was quantified with the LMG metric, which averages order-specific sequential R^2 contributions of each predictor across all permutations of entry into the model (Hussain et al., 2025b). All steps below were repeated for each region and each scenario. In practice this is done by filtering the data to a region×scenario subset and then running the same pipeline.

We first examined the correlation matrix and significance of pairwise correlations, then computed VIF from an initial full model, and finally applied variable clustering (hierarchical clustering of the correlation matrix). In subsequent modeling we retained at most one variable from each highly collinear cluster (e.g., between precipitation and runoff) to stabilize coefficient estimates and avoid

https://doi.org/10.5194/egusphere-2026-3008
Preprint. Discussion started: 2 July 2026

variance inflation. We fit a reduced model after collinearity screening and conducted a Bonferroni outlier test on standardized residuals (Bland and Altman, 1995; Rezaei et al., 2024). Flagged observations (if any) were removed, and the model was re-estimated on the cleaned dataset. This step protects against leverage points that can unduly influence coefficients.

We inspected autocorrelation plots for each retained predictor and the response. Lags were selected when autocorrelation exceeded the 95% confidence bounds (e.g., 1–2 months for temperature, precipitation, and LAI, and 3–4 months for SM depending on region). Only those lags were added to the design matrix. This step captures short-term memory effects and improves fit without resorting to full time-series models.

Minimum, maximum, average, and final R^2 values are summarized in **Tables S3–S5** for all SRM scenarios and their baselines. These tables provide a quantitative measure of model fit quality and confirm that the final lag-enhanced MLRs capture the majority of variance in both AW ($R^2 > 0.99$ in most cases), indicating excellent explanatory performance across regions under each scenario of GHG-emissions (SSP2-4.5 and SSP5-8.5) and SRM (G6-1.5K-SAI, G6solar, G6sulfur and Geo-SAI) scenarios.

3. Results

3.1. Ensemble mean hydroclimate anomalies

Figure 2 illustrates the temporal evolution of ensemble-mean hydroclimatic anomalies under the different forcing scenarios averaged over the combined Central–South Asia and Tibetan Plateau region, while **Table 1** summarizes the corresponding regional mean percent changes over WCA, ECA, TIB, and SAS for 2055–2084 relative to 2015–2034.

Temperature increases markedly under warming (**Figure 2a, b**), with substantially stronger warming in the transient forcing experiments (e.g., SSP5-8.5; +0.81 per decade) than in the temperature-stabilized experiments (+0.26 per decade under SSP2-4.5). G6-1.5K-SAI and Geo-SAI substantially moderate this warming (**Figure 2a, b**). Across the subregions, the TIB exhibits the largest significant warming, followed by ECA, under all scenarios. In contrast, the temperature-stabilized experiments show significant cooling in WCA, ECA, and TIB, whereas the transient forcing experiments show significant warming across all regions (**Table 1**). Precipitation is increasing under warming, mainly concentrated over the Himalayan region (**Figure S1g-l**). Geo-SAI tend to increase it but reduce under G6sulfur (**Figure 2c, d**). Across the subregions, the ECA exhibits significant increase in all scenarios, except in G6-1.5K-SAI, whereas G6solar reduces it in WCA, TIB and SAS. In contrast, the temperature-stabilized experiments show a dominant decrease

https://doi.org/10.5194/egusphere-2026-3008
Preprint. Discussion started: 2 July 2026

in TIB, whereas the transient forcing significantly increases it in ECA, TIB and SAS (**Table 1**). ET is increasing under warming but decreasing under temperature stabilized and transient experiments (**Figure 2e, f**). Across the subregions, the temperature-stabilized experiments show decrease in WCA, ECA, and TIB, whereas the transient experiments show increase in WCA and SAS (**Table 1**).

The AW is increasing under Geo-SAI, whereas it decreases under G6sulfur (**Figure 2g, h**). Across the subregions, the WCA exhibits the largest significant decrease, whereas increase in ECA and TIB (except G6-1.5K-SAI) under all scenarios (**Table 1**). Cryosphere variables display strong sensitivity to forcing pathways. Snowfall and snowmelt increase under stabilized and transient forcing (except G6solar) experiments (**Figure i-l**). Across subregions, the temperature stabilized experiments increase the snowfall and snowmelt while decrease in transient experiments in all regions, with highest significant decrease in SAS, followed by WCA and TIB (**Table 2**). Runoff is increasing under warming but decrease is dominant under stabilized and transient experiments (**Figure 2m, n**). The G6-1.5K-SAI decreases runoff in all regions whereas transient decrease in WCA, while increase in TIB and SAS (**Table 1**). SM is increasing under Geo-SAI and transient experiments (**Figure 2 o, p**). Across subregions, it decreases under G6-1.5K-SAI in all regions, whereas increase (decrease) under G6sulfur, relative to SSP5-8.5 (SSP2-4.5) (**Table 1**). LAI increases across all scenarios, with stronger trends under transient forcing compared to temperature-stabilized cases in the whole and subregions (**Figure 2 and Table 1**).

3.2 Trends and sulfur-normalized hydroclimate responses

Mean temperature (**Figure 3a, j**) show widespread warming under SSP5-8.5 (>0.70 °C decade^{-1}) in the raw trends nearly equal to global increase, while G6solar reduces this by 0.23–0.33 °C decade^{-1}. In sulfur-normalized SAI experiments exhibit distinct cooling efficiencies, with G6-1.5K-SAI producing the strongest cooling per unit sulfur (−0.02 °C decade^{-1} Tg SO_2^{-1}), whereas G6sulfur shows weaker responses and Geo-SAI exhibits near-zero changes in some regions. Precipitation (**Figure 3b, k**) increases under SSP5-8.5, particularly over TIB (up to 27.34 mm decade^{-1}) and SAS, while G6solar moderates these increases. The sulfur-normalized SAI experiments consistently suppress mean precipitation per unit sulfur across regions, with relatively uniform responses among experiments. ET (**Figure 3c, l**) increases strongly under SSP5-8.5 and is partially reduced under G6solar, whereas the sulfur-normalized G6-1.5K-SAI exhibits the largest and most consistent decreases in ET per unit sulfur, while G6sulfur shows weak responses and Geo-SAI shows moderate but spatially variable reductions.

https://doi.org/10.5194/egusphere-2026-3008
Preprint. Discussion started: 2 July 2026

AW (**Figure 3d, m**) increases over ECA, TIB and SAS under SSP5-8.5, while G6solar moderates these patterns. The sulfur-normalized SAI experiments exhibit variable responses, with limited increases in AW per unit sulfur and decline in WCA and TIB under G6-1.5K-SAI and Geo-SAI. Snowfall (**Figure 3e, n**) shows mostly decreasing trends in the raw panel, whereas sulfur-normalized trends indicate small but generally positive changes per unit sulfur in some regions. Snowmelt (**Figure 3f, o**) shows strongly negative raw trends under SSP5-8.5, while G6solar retains negative trends in smaller magnitudes. The sulfur-normalized SAI experiments exhibit contrasting responses: G6sulfur shows the most consistent negative snowmelt trends per unit sulfur, whereas G6-1.5K-SAI is near-zero and Geo-SAI shows mixed responses.

Runoff (**Figure 3g, p**) increases under SSP5-8.5, particularly over TIB (4.13 mm decade^{-1}), while G6solar reduces these increases (−1.38 mm decade^{-1}). The sulfur-normalized SAI experiments show small but regionally contrasting responses per unit sulfur. G6-1.5K-SAI produces decreases over TIB and SAS, whereas G6sulfur and Geo-SAI show weak increases in some regions. SM (**Figure 3h, q**) declines under SSP5-8.5 over TIB and SAS; consistent with global trends, while G6solar partially alleviates this drying. The sulfur-normalized SAI experiments show weak but mixed responses per unit sulfur. LAI (**Figure 3i, r**) increases across all scenarios in the raw trends, with the largest increases under SSP5-8.5, reflecting combined effects of warming and CO_2 fertilization. The sulfur-normalized SAI experiments show small increases per unit sulfur, with G6sulfur exhibiting slightly stronger responses compared to G6-1.5K-SAI and Geo-SAI.

A clear distinction emerges between regional and global responses in both raw and sulfur-normalized trends (**Figure 3a–r**). Regional signals—particularly over TIB and SAS—are substantially larger and more variable than the global mean, whereas global trends are considerably damped, and this pattern persists after normalization, indicating that regional contrasts reflect underlying processes and injection strategy rather than sulfur amount alone. Overall, temperature and ET show the strongest and most consistent responses per unit sulfur, whereas AW, runoff, and SM exhibit weaker and regionally heterogeneous responses. Snowmelt varies substantially among SAI strategies, highlighting sensitivity to both temperature changes and latitudinal forcing. Differences in efficiency are linked to injection strategy, with subtropical injections producing stronger regional cooling responses and equatorial injection leading to weaker or more spatially distributed effects. These results demonstrate that regional hydroclimatic impacts of SAI cannot be inferred from global averages, and that while SAI effectively moderates temperature-driven processes, its ability to restore hydrological conditions is limited and strongly dependent on both injection magnitude and location.

https://doi.org/10.5194/egusphere-2026-3008
Preprint. Discussion started: 2 July 2026

3.3. Changes in regional extremes and annual peak responses

Regional distributions of annual peak hydroclimatic (**Figure 4**), together with percent changes relative to present-day conditions (**Table S6**), reveal contrasting behavior between temperature-stabilized experiments and transient forcing experiments. The peak temperature increases under both SSP2-4.5 and SSP5-8.5 in all regions, are effectively constrained with small deviations across regions in temperature-stabilized experiments, whereas, transient experiments reduce it relative to SSP5-8.5 but retain higher variability (**Figure 4a–b** and **Table S6**). Peak precipitation shows moderate increases under SSP2-4.5 in ECA, TIB and SAS, and substantially larger increases over TIB (13.02%) and SAS (7.53%) under SSP5-8.5 (**Figure 4c–d** and **Table S6**). In the temperature-stabilized experiments, precipitation over the TIB decreases under G6-1.5K-SAI (−5.43%) and Geo-SAI (−0.69%). In the transient forcing experiments, precipitation under G6sulfur (9.75%–10.51%) is lower than under SSP5-8.5 but generally remains higher than under SSP2-4.5, indicating partial suppression of the high-emission response. Peak ET (**Figure 4e–f**) increases under warming across all regions, with stronger increases over TIB and SAS (up to 6.52%). In temperature-stabilized experiments, ET is reduced but shows strong regional variability, while in transient forcing experiments it is partially suppressed relative to SSP5-8.5 but remains regionally variable, with notable reductions in WCA and TIB (**Table S6**).

Peak AW shows strong amplification under SSP5-8.5, particularly over the TIB and SAS (up to 18.76% and 9.44%, respectively) (**Figure 4g–h; Table S6**). In the temperature-stabilized experiments, peak AW decreases over the TIB (2.30% to −4.17%), while over SAS it decreases strongly under G6-1.5K-SAI (−12.20%) but increases under Geo-SAI (+8.91%). In the transient forcing experiments, peak AW over the TIB is lower than under SSP5-8.5 (15.26%) but generally remains higher than under SSP2-4.5 (19.06%) (**Table S6**), indicating partial rather than complete offset of the high-emission signal under G6sulfur and G6solar. Snowfall exhibits regionally mixed responses under warming, with increases in ECA but significant declines in other regions under SSP2-4.5 and SSP5-8.5 (**Figure 4i–j** and **Table S6**). In temperature-stabilized experiments, snowfall increases over WCA, ECA and TIB, while in transient forcing experiments it decreases under G6sulfur and G6solar across WCA, TIB, and SAS. Snowmelt peaks generally decrease under warming, with pronounced reductions over TIB and SAS (down to ~−44% under SSP5-8.5), reflecting reduced snow availability and earlier melt (**Figure 4k–l** and **Table S6**). In temperature-stabilized experiments, snowmelt increases over WCA, ECA and TIB (e.g., ~20%), while it decreases under transient forcings.

https://doi.org/10.5194/egusphere-2026-3008
Preprint. Discussion started: 2 July 2026

Peak runoff exhibits regionally heterogeneous responses under warming, with small changes in WCA and ECA but stronger decreases over TIB and SAS under SSP5-8.5 (**Figure 4m–n** and **Table S6**). In G6-1.5K-SAI, runoff shows decreases but strong increases in WCA, ECA and SAS under Geo-SAI, while in transient forcing experiments it remains variable, with strong increases in TIB and SAS under G6sulfur, relative to SSP2-4.5. SM shows declines in WCA, ECA and TIB under warming (**Figure 4o–p** and **Table S6**). In temperature-stabilized experiments, SM decreases under G6-1.5K-SAI in WCA, TIB, and SAS but increases under Geo-SAI, while in transient forcing experiments SM responses remain small and regionally heterogeneous, indicating incomplete offset of SM changes. Peak LAI increases under warming, with larger increases under SSP5-8.5 (up to 42%) (**Figure 4q–r** and **Table S6**), while temperature-stabilized experiments show reduced responses including decreases over ECA and TIB, and transient forcing experiments exhibit modest, regionally consistent changes with generally significant increases.

3.4. Percent changes in hydroclimatic amplitude

Changes in the amplitude of hydroclimatic variables reflect shifts in the magnitude of seasonal and interannual variability, providing insight into how climate extremes respond to warming and SRM interventions.

Temperature amplitude (**Figure 5a–b**) increases under both SSP2-4.5 and SSP5-8.5 across all regions, with the largest amplification over TIB and SAS. Temperature-stabilized experiments effectively constrain this increase, whereas transient forcings partially reduce amplitude relative to SSP5-8.5 but higher variability exists in TIB and SAS. Precipitation amplitude (**Figure 5c–d**) increases under SSP5-8.5, especially over TIB and SAS. In temperature-stabilized experiments, precipitation amplitude is generally reduced, with notable suppression over TIB under G6-1.5K-SAI and Geo-SAI, whereas transient forcings show partial reductions relative to SSP5-8.5 but retain elevated variability, with mix responses across WCA and ECA. ET amplitude (**Figure 5e–f**) increases under warming. Temperature-stabilized experiments increase ET in TIB and SAS under Geo-SAI, while transient forcing experiments show partial suppression but maintain notable regional variability. AW amplitude (**Figure 5g–h**) shows increase under warming, with temperature-stabilized experiments generally suppress it, particularly G6-1.5K-SAI, whereas transient experiments exhibit mixed responses.

Cryospheric variables show strong sensitivity to forcing pathway. Snowfall amplitude (**Figure 5i–j**) declines under warming. Temperature-stabilized experiments reverse this in WCA, ECA and TIB, whereas transient forcings show continued suppression in WCA and SAS. Snowmelt

https://doi.org/10.5194/egusphere-2026-3008
Preprint. Discussion started: 2 July 2026

amplitude (**Figure 5k–l**) decreases strongly under warming, and it is continued significantly under both temperature-stabilized and transient experiments. Runoff amplitude (**Figure 5m–n**) increases under warming, with increase (decrease) under Geo-SAI (G6-1.5K-SAI), while transient forcing experiments further increase it in G6sulfur relative to SSP585 and decrease under G6solar. SM amplitude (**Figure 5o–p**) declines under warming in WCA and TIB but increases in ECA and SAS. Temperature-stabilized experiments partially offset these changes, while transient experiments show weaker and more heterogeneous responses. LAI amplitude (**Figure 5q–r**) increases under warming across all regions, with the largest amplification over SAS. Both temperature-stabilized and transient experiments maintain positive anomalies, with slightly enhanced variability under some SAI scenarios (e.g., G6sulfur and Geo-SAI).

Overall, warming leads to a broad amplification of hydroclimatic amplitude in temperature, precipitation, ET, AW, runoff, and vegetation, alongside reduced snowfall and snowmelt. Temperature-stabilized experiments effectively constrain variability in temperature-driven processes but produce regionally heterogeneous hydrological responses, with some variables suppressed and others enhanced depending on region and experiment. In contrast, transient forcing experiments provide only partial mitigation, retaining elevated variability and mixed regional responses. Cryospheric variables show strong sensitivity to both forcing pathway and regional temperature changes, while runoff and SM reflect complex interactions among precipitation, ET, and snow processes.

3.5. Seasonal cycle changes

To isolate the effect of SRM from GHG-induced changes, we first describe seasonal responses under GHG-only forcing and then evaluate whether SRM simulations suppress these responses, particularly where GHG-induced changes are statistically significant.

Seasonal cycles (**Figure 6a–d**) show that temperature peaks during June–August across all regions, with warming signals intensifying under higher GHG forcing. Under SSP2–4.5, temperature maxima typically occur in August, whereas SSP5–8.5 produces earlier peaks in July, indicating an advancement of seasonal warming under stronger radiative forcing. Precipitation (**Figure 6e–h**) is dominated by the summer monsoon (July–August) in TIB and SAS, while WCA and ECA exhibit weaker seasonal variability. Both SSP2–4.5 and SSP5–8.5 show precipitation peaks in July across most regions. ET (**Figure 6i–l**) peaks between May-October, with earlier peak timing generally observed under stronger warming, particularly in WCA, ECA, and SAS, while TIB shows consistent July peaks across forcing levels. AW (**Figure 6m–p**) exhibits pre-monsoon maxima in

https://doi.org/10.5194/egusphere-2026-3008
Preprint. Discussion started: 2 July 2026

ECA and July–August peaks in TIB and SAS, with earlier peak timing under GHG warming, particularly under SSP5–8.5. Cryosphere and hydrological processes also respond strongly to GHG forcing. Snowfall (**Figure 6q–t**) and snowmelt (**Figure 6u–x**) seasonal cycles shift earlier under both SSP2–4.5 and SSP5–8.5, consistent with warming-driven earlier snow accumulation and melt onset. Runoff (**Figure 6y–ab**) peaks during May–July in WCA and extends through July–August in ECA, TIB, and SAS, with earlier peaks under higher GHG forcing. SM (**Figure 6ac–af**) peaks during late winter to spring in WCA and ECA, extending into summer in TIB and SAS, while LAI (**Figure 6ag–aj**) shows earlier seasonal maxima under stronger warming.

Relative to their respective GHG baselines, SRM simulations generally moderate and delay GHG-induced seasonal shifts. For temperature (**Figure 6a–d**), G6-1.5K-SAI and Geo-SAI tend to shift peak warming toward later months compared to GHG-only scenarios, while G6 experiments partially offset the earlier peak shifts seen under SSP5–8.5. For precipitation (**Figure 6e–h**), G6-1.5K-SAI and Geo-SAI shift peak timing from July to August in ECA, TIB, and SAS, indicating a partial reversal of GHG-induced seasonal advancement, while G6 experiments maintain July peaks but reduce overall intensity relative to SSP5–8.5. Similar moderation effects are evident for ET and AW, where SRM simulations tend to delay peak responses relative to GHG-only forcing. Cryosphere variables show particularly strong SRM influence: snowfall and snowmelt peaks shift later under G6-1.5K-SAI and Geo-SAI compared to earlier peaks under GHG warming, while G6 simulations moderate but do not fully reverse GHG-driven shifts. Runoff and SM seasonal cycles under SRM also tend to shift toward later peak timing compared to high-emission GHG scenarios. LAI responses indicate delayed peak vegetation activity under SRM relative to high GHG forcing.

Collectively, these results indicate that GHG warming advances seasonal hydroclimatic cycles and intensifies temperature and hydrological responses, while SRM simulations generally act to suppress or delay these GHG-induced changes. This contrast highlights the role of SRM in moderating hydroclimatic responses, particularly in regions and variables where GHG-driven changes are strongest and statistically significant, thereby emphasizing its potential to partially offset future warming-related climate impacts.

3.6. Hydro-climatic drivers of available water (AW) variability

The MLR framework is used to quantify the relative importance of hydroclimatic predictors controlling AW variability (**Figure 7**), under temperature-stabilized and transient forcing experiments. Across all regions, AW variability reflects the combined influence of precipitation

https://doi.org/10.5194/egusphere-2026-3008
Preprint. Discussion started: 2 July 2026

(PCP), temperature (TMP), ET, SM, and LAI, with clear differences emerging between forcing pathways.

In temperature-stabilized experiments (**Figure 7a, c, e, g**), precipitation remains the dominant control on AW variability in ECA, TIB, and SAS followed by temperature and SM, while WCA shows a stronger influence of temperature and ET, indicating enhanced land–atmosphere coupling. In TIB and SAS, the dominance of precipitation is particularly pronounced, reflecting strong dependence on moisture supply even under stabilized temperature conditions. SM contributes as a secondary control in ECA and SAS, while LAI plays a relatively minor but non-negligible role, especially in regions with strong vegetation–water interactions. In contrast, transient forcing experiments (**Figure 7b, d, f, h**) show a more pronounced dominance of precipitation across all regions, indicating that AW variability becomes increasingly controlled by moisture supply under stronger forcing. Temperature and ET contributions remain important in WCA but are generally reduced relative to precipitation in other regions. SM plays a consistent secondary role, particularly in ECA and SAS, while LAI contributions remain small but slightly enhanced under higher forcing scenarios.

Comparing forcing pathways, temperature-stabilized experiments tend to redistribute the relative importance of predictors by reducing the dominance of precipitation and enhancing the role of temperature and ET in some regions (notably WCA), whereas transient forcing experiments maintain or amplify precipitation dominance, indicating that partial compensation of radiative forcing does not fundamentally alter the primary controls on AW variability. Overall, precipitation remains the dominant driver of AW variability across most regions, particularly in ECA, TIB, and SAS, while temperature and ET play a more prominent role in arid and semi-arid regions such as WCA, highlighting that SAI modifies the relative contributions of drivers without fundamentally changing the underlying hydroclimatic controls.

4. Discussion

This study evaluates the impacts of SRM under temperature-stabilized (G6-1.5K-SAI and Geo-SAI), and transient forcing experiments (G6solar and G6sulfur). Using CESM2-WACCM6 simulations, we assess how these contrasting strategies influence future changes in temperature, precipitation, ET, AW, snowfall flux, snowmelt flux, runoff, SM, and LAI across WCA, ECA, TIB, and SAS for the period 2055–2084 relative to present-day conditions (2015–2034), and their effects on regional water availability.

https://doi.org/10.5194/egusphere-2026-3008
Preprint. Discussion started: 2 July 2026

4.1 Hydroclimatic Intensification and Seasonal Shifts Under GHG Warming

Global GHG-emission–driven warming leads to widespread intensification of hydroclimatic processes across Asia (Miao et al., 2020), with increasing temperature, ET, and hydrological variability, accompanied by regionally varying precipitation and SM responses. Consistent with previous studies, warming is particularly pronounced over WCA, ECA, and SAS (Ren et al., 2024; Ullah et al., 2023c), while precipitation increases are projected across large parts of Asia, particularly in WCA and SAS (Ren et al., 2024; Feng et al., 2014; Xu et al., 2017). GHG forcing-induced increases in ET are also projected, especially over eastern Asia (Ren et al., 2024). However, SM responses remain spatially heterogeneous, with long-term SM declines reported across parts of Asia despite increasing precipitation in some regions (Cheng et al., 2015; Berg et al., 2017). These findings highlight the dominant role of temperature-driven evaporative demand in controlling regional hydrology and water availability under warming conditions.

Under SSP2–4.5 and SSP5–8.5, hydroclimatic variables show strong regional contrasts reflecting differences in moisture supply, cryosphere processes, and land–atmosphere coupling. The GHG forcing scenarios consistently intensify hydroclimatic variability, and cryosphere melt, particularly over the TIB and SAS, while exacerbating hydrological stress in WCA and ECA (**Figure 3**). Seasonal cycles also become amplified under warming, with earlier seasonal peaks and enhanced amplitude in temperature, ET, runoff, SM, and AW, indicating increased hydroclimatic seasonality and extremes (**Figure 4-5**). These feedbacks are strongly interconnected, with temperature controlling ET and SM depletion, while precipitation governs surface water inputs and vegetation growth. Such interactions amplify water loss in warm-lands such as SAS and intensify snowmelt-driven variability in high-elevation regions such as TIB. From 1981 to 2017, Tarbela and Mangla reservoirs in Pakistan showed significant declines in water extent, with stronger losses at Mangla Reservoir, particularly during March–June (Akhtar and Athar, 2019). Consistent with these observed declines, projected warm-season temperature increases coupled with decreases in winter precipitation and runoff during 2071–2100 pose significant threats to water security in SAS (Khan, 2022). Similarly, rising temperatures have accelerated glacier retreat in Central Asia, and this glacier loss, together with shifts in precipitation patterns, is expected to alter regional flow regimes (Savitskiy et al., 2008), consequently affecting the irrigation, which accounts for more than 90% of all water intake from the region's rivers (Ibatullin et al., 2009). Global warming–driven cryosphere melt and thaw are increasingly disrupting the volume and timing of water supply from High Mountain Asia, threatening downstream food and energy systems and highlighting the need for climate-resilient dam design, and maintenance (Li et al., 2022a).

https://doi.org/10.5194/egusphere-2026-3008
Preprint. Discussion started: 2 July 2026

For SSP2-4.5 and SSP5-8.5, snowfall and snowmelt responses show strong regional contrasts that reflect the balance between temperature-driven phase and moisture availability (**Figure 3**). Under the high GHG-emission SSP5-8.5 scenario, reduced snowfall and accelerated snowmelt over high-elevation regions indicate a shift from solid to liquid precipitation and accelerated cryosphere loss (Barnett et al., 2005; Berghuijs et al., 2014; Deng et al., 2017; Li et al., 2023; Li et al., 2024). This response is consistent with intensified warming and increased energy availability, which promote earlier and more rapid melt processes (Barnett et al., 2005). Heterogeneous glacier retreat from the Himalaya and Karakoram region is altering streamflow patterns, increasing the risk of glacial-lake outburst floods and worsening future flooding and water shortages, with potentially severe impacts on downstream populations, infrastructure, hydropower, and major irrigated agricultural systems by making water flows more extreme and unpredictable (Nie et al., 2021). The strongest peak increases occur over the TIB under SSP5-8.5 (**Figure 4**), where the hydrological system is highly sensitive to warming. For instance, GHG-induced global warming accelerates hydrological cycles, leading to a significant increase in hydrological wet extremes in the TIB (Wang et al., 2023b), especially low streamflow would increase more significantly (Zhong et al., 2018). Such intensification in extreme events has triggered the risks of a significant increase in heatwave and extreme precipitation events in the TIB (Zhang et al., 2025; Jiang et al., 2025). The largest peak changes in hydroclimate variables (particularly temperature, precipitation, AW, runoff, and LAI) occur in the TIB and SAS, even though its warming magnitude is comparable to other regions (**Figure 4**).

Warming-induced hydroclimatic intensification also strongly influences monsoonal systems. Under GHG forcing, earlier runoff peaks with increased and greater amplitude in runoff, temperature, SM, and LAI are observed across the Asian monsoon domain (**Figure 4-5**), consistent with previous studies showing that warming strengthens atmospheric moisture transport and intensifies monsoon-driven hydrological extremes (Bal et al., 2019). The TIB and SAS exhibit the strongest summer peaks in precipitation, runoff, and AW, reflecting intensified monsoonal activity and enhanced warming over high-elevation and monsoon-dominated regions. In contrast, WCA and ECA exhibit weaker seasonal peaks due to their arid to semi-arid continental climates and limited moisture supply.

Several works have shown that wet regions tend to become wetter and dry regions drier under GHG-induced warming, a response consistent with the thermodynamic amplification of the existing hydrological cycle (Held and Soden, 2006; Ipcc, 2021). In high-elevation and monsoon-dominated regions, increased precipitation and cryosphere melt contribute to higher AW

https://doi.org/10.5194/egusphere-2026-3008
Preprint. Discussion started: 2 July 2026

(Immerzeel et al., 2010; Lutz et al., 2014). In contrast, arid regions experience reduced SM and runoff due to enhanced ET and limited precipitation replenishment (Li et al., 2025; Liu et al., 2025). Despite precipitation increases in some regions, warming-driven increases in ET and cryosphere melt often offset gains in water availability. This is particularly evident in WCA and ECA, where rising evaporative demand and declining SM contribute to increasing water stress. Our findings from the regions with a wide-range of climate regimes of moisture-limited Central Asia, cryosphere-influenced TIB, and monsoon-dominated SAS suggest that under GHG warming, regional water availability is governed not only by precipitation changes but also by energy-limited processes controlling ET and SM dynamics.

Consistent with MLR analysis, AW variability under warming is not controlled by precipitation alone but by a complex interplay among precipitation, temperature, SM, and LAI (**Figure 7**), aligns with findings from Rezaei et al. (2025a). Although precipitation remains the dominant driver of AW across most regions, particularly with warm climate, regional differences persist in the combination of controlling variables. For example, AW in the TIB is influenced by precipitation, temperature, SM, followed by snowfall and snowmelt, whereas in warmer and wetter regions such as ECA and SAS, precipitation and SM dominate AW variability. In contrast, the arid WCA region exhibits a more balanced control among temperature, precipitation, ET, SM, and LAI, consistent with findings from other semi-arid regions in the Middle East and North Africa (Rezaei et al., 2024).

Overall, GHG warming accelerates hydroclimatic cycles, enhances seasonal amplitude, and intensifies cryosphere decline, with the strongest impacts occurring in high-elevation and monsoon-dominated regions. These warming-driven hydroclimatic responses establish the baseline climate trajectory against which potential SRM-induced modifications are evaluated.

4.2 Effectiveness of SRM in Suppressing GHG-Induced Changes

SRM scenarios can mitigate global warming impacts by reducing extreme heat events (Dagon and Schrag, 2017), stabilizing precipitation patterns (Liu et al., 2021), and offsetting temperature rise (Tilmes et al., 2020). As designed by the experiment, temperature-stabilized experiments effectively constrain warming across regions, whereas transient forcing experiments partially compensate GHG forcings, leading to residual variability in hydrological responses despite overall cooling (**Figure 2–3**).

Temperature-stabilized experiments show a stronger and consistent reduction in temperature across all regions, leading to a clearer moderation of hydrological intensification, whereas transient

https://doi.org/10.5194/egusphere-2026-3008
Preprint. Discussion started: 2 July 2026

forcing experiments provide only partial cooling and retain greater variability in hydrological responses (**Figure 4**). Despite this cooling, both pathways exhibit amplified LAI peak changes, highlighting the persistent influence of elevated CO_2 and regionally varying land–atmosphere interactions. As explained by Rezaei et al. (2024), cooling-induced reductions in ET have limited effectiveness in drier regions, where water availability is primarily constrained by moisture supply rather than energy demand. This is consistent with our results, where both temperature-stabilized and transient forcing experiments alleviate warming but only partially improve precipitation, AW, and SM in WCA and ECA. These limited hydrological responses persist despite differences in sulfur injection magnitude and strategy (**Table S2**), indicating that in moisture-limited regions, increasing or redistributing SAI forcing does not substantially enhance water availability.

SAS shows more consistent improvements under temperature-stabilized experiments, where reduced heat extremes and relatively regulated precipitation contribute to improved hydroclimatic conditions, whereas, transient forcing experiments provide only partial mitigation, with residual variability in temperature and precipitation limiting the overall hydrological benefits. These differences are consistent with the experimental design (**Table S2**), where temperature-stabilized scenarios (e.g., G6-1.5K-SAI and Geo-SAI) employ higher or more spatially distributed sulfur injection (≈11.7–35 Tg SO_2 yr^{-1}) to maintain temperature targets, while transient forcing experiments (e.g., G6sulfur) use lower or equatorially concentrated injections (≈21 Tg SO_2 yr^{-1}), leading to weaker and more regionally variable hydroclimatic responses. This suggests that, despite broader tropical and subtropical trade-offs, SAS may experience comparatively favorable outcomes under temperature-stabilized SRM pathways.

The findings of Abiodun et al. (2021), based on the Geoengineering Large Ensemble (GLENS, SAI+RCP8.5) over Africa, are broadly consistent with our results in showing that SAI can effectively moderate temperature and ET in tropical regions. However, while GLENS indicates possible overcompensation of precipitation and resulting net water deficits in some tropical areas, our results suggest that such overcorrection is less pronounced in SAS under both temperature-stabilized and transient forcing experiments. This contrast likely reflects not only differences in sulfur burden and spatial deployment (**Table S2**), but also the latitude of injection and the underlying GHG-forcing baseline. Recent studies show that equatorial injection tends to enhance tropical lower-stratospheric heating reduces tropical precipitation, and is less efficient than subtropical injection (Henry et al., 2024; Wells et al., 2024; Bednarz et al., 2023). G6sulfur represents a tropical injection strategy, whereas G6-1.5K-SAI is implemented with off-equatorial injection and Geo-SAI uses multi-latitude injection, so part of the difference in hydroclimatic

https://doi.org/10.5194/egusphere-2026-3008
Preprint. Discussion started: 2 July 2026

response may arise from injection latitude rather than sulfur amount alone (Richter et al., 2022; Tilmes et al., 2020). In addition, G6-1.5K-SAI is implemented relative to an SSP2-4.5 background, whereas G6sulfur and Geo-SAI are evaluated against SSP5-8.5, and previous work has shown that SAI outcomes depend on the baseline state selected for comparison as well as on the injection strategy itself (Tilmes et al., 2020; Visioni et al., 2021; Visioni et al., 2023; Richter et al., 2022). Accordingly, contrasts among GLENS and the CESM2 experiments considered here should be interpreted as the combined effect of baseline forcing, injection latitude, and deployment design, rather than as a simple consequence of aerosol loading alone.

Building on regional evidence of solar geoengineering impacts, Patel et al. (2023) demonstrated that SAI can substantially alter temperature and precipitation extremes, sometimes leading to overcompensation effects. Such behavior is more likely in temperature-stabilized experiments, where stronger cooling can suppress warming-driven hot extremes but may also introduce localized overcooling. This is consistent with GLENS-type experiments, which employ relatively high and dynamically adjusted sulfur injection rates (typically reaching ~10–50 Tg SO_2 yr^{-1}), allowing strong radiative forcing that can lead to overcompensation in some regions. In contrast, transient forcing experiments tend to exhibit more moderate responses, with reduced likelihood of overcompensation but greater residual variability in extremes. Recent findings of Zhang et al. (2024a), using the GFDL-ESM4.1 model under an overshoot scenario (SSP5-3.4-OS), further support the pathway-dependent and regionally variable nature of SRM impacts. Their simulations show substantial global cooling (~1.5 °C) accompanied by reductions in precipitation and shifts in tropical rainfall patterns, particularly toward the Northern Hemisphere. These results are consistent with GLENS-based evidence of uneven hydrological responses. In this context, our results suggest that while some tropical regions may experience water deficits under both forcing pathways, SAS shows comparatively more favorable responses—particularly under temperature-stabilized experiments—where reduced heat extremes and relatively stable precipitation provide potential hydroclimatic benefits despite broader regional trade-offs.

Across both GHG forcing pathways, SRM moderates cryosphere loss through enhanced snowfall and reduced snowmelt, particularly over the TIB, although the magnitude of this response is more pronounced under temperature-stabilized conditions. The potential benefits of SRM are particularly relevant for water resources, agriculture, and food security in dry regions such as Central Asia. In these moisture-limited environments, even modest reductions in temperature and evaporative demand can have disproportionate impacts compared to wetter regions, where SRM primarily moderates excess moisture. By lowering temperature and reducing atmospheric evaporative

https://doi.org/10.5194/egusphere-2026-3008
Preprint. Discussion started: 2 July 2026

demand, both temperature-stabilized and transient forcing experiments can alleviate some drought stress in certain regions; however, these benefits are not uniform, as SAI may also intensify drought in other areas, with tropical Africa projected to experience severe drying (Liu et al., 2024), and summertime SM reduced by 42 ± 11 kg m^{-2} in India and 27 ± 16 kg m^{-2} in the Amazon, mainly due to decreased precipitation (Cheng et al., 2019). However, the extent of these benefits remains constrained by precipitation availability, particularly in transient forcing experiments where incomplete compensation of GHG forcing limits hydrological recovery. Given that arid and semi-arid regions are highly sensitive to small increases in temperature and ET (Huang et al., 2016; Xia et al., 2017a; You et al., 2018), the effectiveness of SRM in these regions depends critically on its ability to suppress warming without further reducing already limited precipitation.

However, cooling does not translate uniformly into hydrological recovery (Rezaei et al., 2025a), as persistent drying and reductions in AW and SM continue in WCA and ECA under both temperature-stabilized and transient forcing experiments (**Figure. 2–4, 7**). While temperature-stabilized experiments more effectively constrain warming and shift hydroclimatic peak timing closer to present-day conditions, transient forcing experiments retain greater variability and less consistent recovery. This distinction is particularly relevant for existing water infrastructure in Central Asia, where dams, reservoirs, and irrigation systems are traditionally been designed under the assumption of stationary climate conditions, relying on historical hydroclimatic variability (Milly et al., 2008; Yao et al., 2021). However, GHG-induced warming has already altered the timing, magnitude, and reliability of water supply through shifts in snowmelt, glacier decline, and increasing ET (Barnett et al., 2005; Milly et al., 2008). Temperature-stabilized experiments help in the non-stationary pressures, potentially extending the operational reliability of existing infrastructure. For example, relative to SSP5-8.5, SRM reduces warming in WCA, with the strongest cooling under Geo-SAI and G6-1.5K-SAI, while ET is strongly suppressed (**Table 1**). Despite these improvements, incomplete hydrological recovery under transient forcing highlights that reduced temperature alone is insufficient to fully restore water availability in moisture-limited regions.

Temperature-stabilized experiments produce a stronger and more consistent reduction in hydroclimatic variability, whereas transient forcing experiments retain greater residual variability (**Figure 2**). As a result, feedbacks vary regionally, amplifying water loss in SAS and intensifying snowmelt-driven variability in colder regions such as the TIB. Under SRM, ET peak and amplitude are more effectively reduced in cooler regions like TIB and ECA, while SAS retains relatively high ET amplitude due to persistent warmth and sufficient moisture supply (**Figure 2, 5**). Cryosphere

https://doi.org/10.5194/egusphere-2026-3008
Preprint. Discussion started: 2 July 2026

responses also show strong regional contrasts: snowfall and snowmelt decrease in WCA and SAS but increase in the TIB, reflecting differences between hot-dry and cold regions, with clearer suppression and recovery patterns under temperature-stabilized experiments and more heterogeneous responses under transient forcing (**Figure 7**).

Significant increases of SM amplitude in ECA and TIB reflect amplified seasonality under SRM scenarios, associated with lower temperatures and higher precipitation peaks (**Figure 2**), with stronger and more consistent amplification under temperature-stabilized experiments. Moreover, G6-1.5K-SAI and G6solar significantly decrease AW amplitude in WCA and ECA, while G6sulfur is more effective in TIB and SAS, likely due to cooler temperatures, higher precipitation, and elevated SM; this contrast highlights pathway-dependent responses, where temperature-stabilized experiments suppress variability more effectively. However, increasing LAI amplitude is driven by reduced ET and sufficient moisture availability (**Figure 2, 5**). The larger increase in LAI over the TIB under both GHG and SRM scenarios likely reflects the fact that SRM reduces temperature but does not reduce atmospheric CO_2 concentrations, allowing CO_2-induced vegetation expansion to persist (Rezaei et al., 2025a). This effect is evident under both forcing pathways, although it is more pronounced under temperature-stabilized conditions where cooling enhances moisture availability. As a result, vegetation increases in this cold-wet region are not fully suppressed by SRM despite reduced warming.

SRM approaches are designed to modify Earth's radiative balance in order to temporarily compensate for GHG-driven warming and help keep global temperature rise below 1.5°C relative to preindustrial levels (Ipcc, 2018; Visioni et al., 2022). In Central Asia, for example, increasing temperatures and glacier retreat have worsened water scarcity (Miao et al., 2020), and climate intervention strategies may help reduce pressure on water resources by moderating future declines and supporting more sustainable water availability. Likewise, in SAS, extreme heat and monsoon variability have increased risks to agriculture and food security (Ullah et al., 2023b; Ullah et al., 2023a), while SRM scenarios may help lessen these risks by reducing temperature extremes and improving precipitation stability. These interpretations are supported by Hussain et al. (2025a), who reported decreases in temperature (−0.62°C) and precipitation (−0.02 mm day^{-1}) under solar geoengineering scenarios in SAS during 2020–2069. SRM scenarios may also offset warming-induced changes in hydrological variables and potentially enhance vegetation cover (**Figure 2-5**), which is consistent with findings reported for the eastern Middle East (Rezaei et al., 2024). Beyond climate-related benefits, such changes may also carry important implications for human health, including reduced malaria transmission risk (Hussain et al., 2024a).

https://doi.org/10.5194/egusphere-2026-3008
Preprint. Discussion started: 2 July 2026

In contrast to the warming-driven cryosphere decline under SSP5-8.5, aerosol-based SRM scenarios such as G6sulfur and Geo-SAI show increased snowfall and suppressed snowmelt over ECA, TIB, and SAS (**Figure 3e–f**), with more consistent responses under temperature-stabilized experiments and greater variability under transient forcing. This response is primarily linked to SRM-induced surface cooling relative to SSP2-4.5 and SSP5-8.5 (**Figure 3a**), which favors snowfall over rainfall and reduces the energy available for melt processes. In addition, enhanced stratospheric aerosol loading reduces incoming shortwave radiation, lowering surface temperatures and delaying seasonal melt onset. Because the TIB region is highly temperature sensitive and influenced by elevation-dependent warming (Meng et al., 2023; Yang et al., 2025), even significant cooling under G6-1.5K-SAI (-10.3%), G6solar (182% to 66.8%), G6sulfur, and Geo-SAI (−1.8%) (**Table 1**) relative to their baselines can substantially shift precipitation phase and snow persistence. This effect is more pronounced under temperature-stabilized experiments, while transient forcing shows weaker but still notable suppression of melt. As a result, SRM partially recovers cryosphere processes in the TIB by enhancing snowfall and reducing melting rate compared to high-emission scenarios. In WCA and ECA, snowfall responses remain weaker and more variable, reflecting lower cryosphere sensitivity and stronger dependence on precipitation variability. Overall, SRM cooling helps maintain precipitation in solid form and delays melt timing, particularly over the TIB where cryosphere–hydrology coupling is strongest.

SRM scenarios counteract runoff peaks, restoring timing and reducing variability in most hydrological variables (**Figure 4–5**), with stronger decrease under temperature-stabilized experiments and more variable responses under transient forcing. This regional suppression is consistent with broader evidence from the GLENS, which shows that SRM suppresses the hydrological cycle relative to the baseline, with end-of-century decreases of 12 ± 5 mm yr^{-1} and 18 ± 2 mm yr^{-1} in the global mean (Cheng et al., 2019). Consistent with this, SAI partially offsets reductions in mean terrestrial water storage in wetter regions, primarily through significant cooling and the resulting decrease in ET relative to SSP5-8.5, but shows no significant influence on the increased terrestrial water storage in drier regions (Rezaei et al., 2024). The pronounced reduction in peak runoff over TIB (−12.3%), and SAS (−47.9%) under Geo-SAI highlights the strong sensitivity of monsoon-driven systems, where hydrological responses are tightly coupled with vegetation and precipitation dynamics. This may be linked to substantial increases in LAI under SSP scenarios that are not fully suppressed by SRM, as these interventions reduce temperature through increased albedo but do not lower atmospheric CO_2 concentrations. Elevated CO_2 continues to enhance vegetation growth, sustaining higher LAI under SAI scenarios (Rezaei et al.,

https://doi.org/10.5194/egusphere-2026-3008
Preprint. Discussion started: 2 July 2026

2025a). Several studies suggest that while SRM moderates global warming, it introduces complex and regionally heterogeneous hydrological responses (Tan et al., 2024). For instance, slight surface cooling across the SAS monsoon region may coincide with strengthened atmospheric circulation but altered precipitation patterns, leading to drier conditions over parts of India under SAI (Bhowmick et al., 2021). Consistent with this, temperature-stabilized experiments more effectively reduce hydrological fluxes in wetter regions (SAS and TIB), whereas transient forcing experiments retain higher variability due to incomplete forcing compensation. In contrast, SRM effects in drier regions (WCA and ECA) are more stabilizing, primarily through reduced temperature and enhanced water retention (**Figure 3**).

SAI has the potential to weaken both average and extreme summer monsoon conditions through mechanisms linked to reduced stratospheric warming, weaker subtropical jet streams, modified wave activity, and a less intense Asian Summer Monsoon Anticyclone (ASMA) (Asutosh et al., 2025). Long-term observational evidence similarly points to a decline in ASMA strength, primarily associated with anthropogenic aerosol forcing, which alters the meridional temperature gradients over Eurasia (Qie et al., 2025). Moreover, increased aerosol optical depth from human activities has contributed to a weakening of the East Asian Summer Monsoon by reducing land–sea thermal and pressure contrasts, along with evaporation and surface radiation (Lang et al., 2025).

The reduction in peak precipitation and AW over SAS and the TIB suggests that aerosol interventions moderate monsoon intensity and associated runoff surges, potentially alleviating flood risks but also reducing water availability during peak demand seasons (Asutosh et al., 2025), with stronger suppression under temperature-stabilized experiments and more moderate reductions under transient forcing. SRM scenarios, especially G6-1.5K-SAI, markedly suppress precipitation peaks over the TIB toward present-day levels, while G6solar, G6sulfur, and Geo-SAI also reduce projected increases. This interpretation aligns with previous studies indicating that aerosol interventions can suppress monsoon rainfall (Ricke et al., 2023), and reduce surface runoff (Rezaei et al., 2025a). Moreover, stratospheric heating associated with aerosol interventions may intensify regional drying (Xia et al., 2017b), further contributing to reduced hydrological fluxes. Collectively, these findings suggest that while SRM moderates hydroclimatic extremes, it may also constrain water availability in monsoon-dependent regions such as SAS, particularly under temperature-stabilized conditions where stronger cooling leads to greater suppression of precipitation peaks, whereas transient forcing retains higher variability in water availability. Furthermore, SM shows decreasing amplitude under G6-1.5K-SAI, G6solar, and G6sulfur, with smaller changes under Geo-SAI in WCA, indicating enhanced water retention and reduced

https://doi.org/10.5194/egusphere-2026-3008
Preprint. Discussion started: 2 July 2026

evaporative losses under cooling (**Figure 5g**). These results align with prior studies (Bala et al., 2008; Robock et al., 2008; Kravitz et al., 2013b; Rezaei et al., 2025a), highlight that SRM impacts remain spatially heterogeneous, with stronger effects in temperature-controlled cold-region of TIB and comparatively weaker responses in drier region of WCA, underscoring the need for region-specific assessments of geoengineering outcomes.

Generally, SRM scenarios reverse the increased peaks in most hydroclimatic variables (except LAI) toward present-day conditions, with temperature-stabilized experiments showing a more complete restoration compared to partial recovery under transient forcing. The regional contrast observed in this study is consistent with regime-dependent SRM responses, where cryosphere- and monsoon-influenced regions such as the TIB and SAS exhibit stronger hydroclimatic sensitivity and recovery, particularly under temperature-stabilized conditions, while drier regions of Central Asia show persistent SM deficits and limited hydrological recovery across both forcing pathways, with weaker mitigation under transient forcing. This highlights that SRM effectiveness depends strongly on baseline hydroclimatic regime rather than producing a uniform wetting or drying response.

4.3 Caveats and Limitations

Despite providing a comprehensive regional assessment of hydroclimatic responses to SRM across WCA, ECA, TIB and SAS using several SRM experiments, several limitations should be acknowledged. First, this analysis is based on simulations from a single Earth system model (CESM2–WACCM6), and although CESM2 represents significant improvements over earlier model generations (Danabasoglu et al., 2020), uncertainties remain due to structural model biases and limited representation of regional hydroclimatic processes. In particular, the relatively coarse spatial resolution (~1°) constrains the ability to fully resolve complex topography, glacier dynamics, land–atmosphere feedbacks, and localized precipitation processes across the TIB and surrounding mountain systems, which are essential for accurately capturing cryosphere–hydrology coupling and region-specific hydroclimatic sensitivity to warming and SRM-induced cooling.

This study used monthly data, which may smooth short-term variability and limit representation of extreme hydroclimatic events, intra-seasonal variability, and peak timing shifts. Many key processes, including extreme precipitation, rapid snowmelt, and short-duration runoff events, occur at daily or sub-daily timescales and may respond differently to SRM forcing than monthly means suggest. Future work using daily or sub-daily simulations would improve assessment of monsoon variability, extreme event suppression, seasonal transition timing, and hydrological threshold responses under SRM and warming scenarios. While the study evaluates hydroclimatic variables

https://doi.org/10.5194/egusphere-2026-3008
Preprint. Discussion started: 2 July 2026

and AW drivers, it does not explicitly incorporate dynamic glacier mass balance modeling, groundwater storage responses, or socio-hydrological feedbacks, potentially influencing the real-world effectiveness of SRM in reducing water stress and hydroclimatic extremes in vulnerable dry and cryosphere-dependent regions.

Furthermore, the hydrological impacts of SAI can vary depending on the climate model used and the design of the deployment strategy (Jones et al., 2018; Bednarz et al., 2023; Laakso et al., 2024; Zhang et al., 2024b; Rezaei et al., 2025a). Runoff changes are particularly linked to evapotranspiration processes. In CESM2, the CLM5 land component represents advanced vegetation–hydrology interactions, including plant hydraulic processes and dynamic stomatal regulation (Lawrence et al., 2019; Fisher et al., 2019). Although these features enhance the model's physical representation, CLM5 may produce excessive greening and transpiration responses under elevated CO_2 conditions, especially in humid ecosystems such as the Amazon (Cordak et al., 2025), which could lead to an overstatement of runoff reductions. Therefore, future work using multi-model comparisons or dedicated sensitivity experiments is required to test the reliability of these projected hydrological responses under SAI.

Future research should prioritize multi-model ensemble assessments to evaluate robustness and reduce structural uncertainty. Higher-resolution regional convection-permitting simulations would improve representation of orographic precipitation, snow processes, and land–atmosphere coupling across the Asian Water Tower, and so would. Coupling SRM simulations with dynamic hydrological, glacier, and groundwater models. Finally, integrating extreme-event analysis, compound hazard risk, and statistical significance–based suppression metrics would help better quantify where and when SRM can meaningfully offset GHG-induced hydroclimatic changes.

5. Conclusions

This study presents a comprehensive assessment of future mean and peak hydroclimatic changes, seasonal cycles, and drivers across heterogeneous climate regimes under warming (SSP2-4.5 and SSP5-8.5) and SRM scenarios (G6-1.5K-SAI, G6solar, G6sulfur, and Geo-SAI) using CESM2-WACCM outputs. The analysis explicitly considers (i) dry, moisture-limited regions of Central Asia (WCA and ECA), where precipitation is concentrated during the cold season; (ii) cold-wet, cryosphere-influenced regions such as the TIB), which experience high snowfall contributions but receive most precipitation during summer; and (iii) warm-wet, monsoon-dominated SAS, where precipitation is strongly concentrated during the summer monsoon. Across these regimes, SRM

https://doi.org/10.5194/egusphere-2026-3008
Preprint. Discussion started: 2 July 2026

demonstrates substantial potential to moderate hydroclimatic extremes, particularly in temperature-sensitive and precipitation-driven systems.

Temperature shows the most robust response, with pronounced warming under SSP5-8.5 and the largest regional sensitivity over TIB and ECA, whereas the temperature-stabilized experiments substantially suppress it. Precipitation generally increases under warming, ET tends to increase under the baseline warming pathways but is reduced in several geoengineering experiments, and AW shows regionally contrasting responses, with strong declines in WCA but increases in parts of ECA and TIB. Snowfall and snowmelt are generally reduced under transient warming, particularly over SAS, WCA, and TIB, while runoff and SM exhibit mixed regional behavior. In contrast, LAI increases consistently across all scenarios

GHG-emission scenarios, particularly SSP5–8.5, substantially amplify peak hydroclimatic responses, with stronger amplification occurring in wet and cryosphere-influenced regions (TIB and SAS) compared to dry, moisture-limited Central Asian regions. Peak temperature increases under SSP2–4.5 and SSP5–8.5, accompanied by strong increases in ET, precipitation, and AW, along with accelerated cryosphere melt and enhanced vegetation activity. In contrast, dry regions (WCA and ECA) show smaller precipitation and AW amplification but remain highly sensitive to warming-driven ET increases and SM losses. SRM scenarios reduce hydroclimatic amplification across all regimes, with strongest stabilization in cold-wet and monsoon-dominated regions. G6-1.5K-SAI shows the strongest overall suppression, followed by G6solar and G6sulfur, while Geo-SAI shows more regionally variable responses. When evaluated per unit sulfur injected, G6-1.5K-SAI also exhibits the highest cooling and hydroclimatic efficiency per Tg SO_2, indicating that its stronger response is not solely due to total sulfur loading but also reflects a more effective injection strategy.

Warming leads to a broad amplification of hydroclimatic amplitude in temperature, precipitation, ET, AW, runoff, and vegetation, alongside reduced snowfall and snowmelt. Temperature-stabilized experiments effectively constrain variability in temperature-driven processes but produce regionally heterogeneous hydrological responses, with some variables suppressed and others enhanced depending on region and experiment. In contrast, transient forcing experiments provide only partial mitigation, retaining elevated variability and mixed regional responses. Cryospheric variables show strong sensitivity to both forcing pathway and regional temperature changes, while runoff and SM reflect complex interactions among precipitation, ET, and snow processes.

https://doi.org/10.5194/egusphere-2026-3008
Preprint. Discussion started: 2 July 2026

Precipitation remains the dominant control on AW under both warming and SRM scenarios, indicating that SRM primarily modifies hydroclimatic magnitude rather than fundamentally altering regional water-cycle controls. Relative to SSP5–8.5, SRM scenarios generally reduce temperature and hydroclimatic variability, although effectiveness varies by climate regime. In dry, moisture-limited regions (WCA and ECA), SRM provides only partial stabilization and cannot fully suppress SM deficits and precipitation-driven variability. In contrast, in the cold-wet TIB, SRM effectively suppresses temperature- and cryosphere-driven influences but can enhance SM. In warm-wet, monsoon-dominated SAS, SRM can enhance precipitation- and land-surface-driven controls, increasing SM and LAI relative to baseline warming. However, sulfur-normalized results demonstrate that hydrological responses such as AW, runoff, and SM show limited and regionally heterogeneous changes per unit sulfur, indicating that increased sulfur injection does not translate linearly into improved water availability.

Overall, the results highlight that SRM effectiveness depends not only on total sulfur injection but also on the efficiency of the intervention per unit sulfur and the deployment strategy. While SRM effectively moderates temperature-driven processes, its hydrological benefits remain limited and spatially variable, particularly in moisture-limited regions. Evaluating SRM performance using sulfur-normalized metrics provides a more robust basis for comparing intervention strategies than absolute responses alone. Consequently, SRM provides partial hydroclimatic regulation but does not uniformly offset regional water stress, especially in semi-arid transition regions of Central Asia, and its overall efficacy depends strongly on both injection magnitude and spatial design.

Data availability. The outputs for SSP2-4.5, and SSP5-8.5, G6solar and G6sulfur scenarios are freely available via the website: https://aims2.llnl.gov/search/cmip6/ (Petrie et al., 2020). The outputs for G6-1.5K-SAI scenarios are freely available at https://gdex.ucar.edu/datasets/d651059/dataaccess/ (Richter et al., 2022). The SSP5-8.5-SAI data are publicly accessible at https://gdex.ucar.edu/datasets/d651024/# (Tilmes, 2024).

Author contributions AH: Conceptualisation, methodology, software, validation, formal analysis, data curation, writing – original draft, visualisation. HL: Conceptualisation, validation, writing – review and editing, funding acquisition AR: Conceptualisation, methodology, writing – review and editing PZ: writing – review and editing, project administration, DV: Conceptualisation, writing – review and editing, GX, CY, YM, and TC writing – review and editing, QL: project administration

Conflict of interest

https://doi.org/10.5194/egusphere-2026-3008
Preprint. Discussion started: 2 July 2026

The contact author has declared that none of the authors has any competing interests.

Funding. This work was supported in part by the National Natural Science Foundation of China (No. 42371337), the Guangdong Basic and Applied Basic Research Foundation (No. 2024A1515011388), the Shenzhen Science and Technology Program (No. JCYJ20230808105709020 and JCYJ20240813142621029), the Guangdong Major Project of Basic and Applied Basic Research (No. 2023B0303000017), the Disciplines Breakthrough Project in Aerospace Information and Spatiotemporal Intelligence， MOE， China, Shenzhen Key Laboratory Program (SYSPG20241211173845013), and Scientific Foundation for Youth Scholars of Shenzhen University (No. 806-000034080293).

Acknowledgements. We used a generative AI tool (Deepseek) to assist with language polishing and expression refinement.

Reference:

Abiodun, B. J., Odoulami, R. C., Sawadogo, W., Oloniyo, O. A., Abatan, A. A., New, M., Lennard, C., Izidine, P., Egbebiyi, T. S., and MacMartin, D. G. Potential impacts of stratospheric aerosol injection on drought risk managements over major river basins in Africa. Clim. Change, 169(3), 31, 2021.

Agada, J., Da-Allada, C., Bocco-Koube, M., Baloïtcha, E., Ayissi, F., Mekonou-Tamko, L., Tilmes, S., and Worou, L. Potential impact of stratospheric aerosol geoengineering on sea surface salinity in the eastern tropical Atlantic Ocean. Environ. Res.: Clim., 4(3), 035009, 2025.

Akhtar, I. u. H. and Athar, H. Contribution of changing precipitation and climatic oscillations in explaining variability of water extents of large reservoirs in Pakistan. Sci. Rep., 9(1), 19022, 2019.

Akram, M., Khan, F., Ullah, H., Ali, S., and Hussain, A. Enhancing Drought Risk Assessment in the Punjab, Pakistan: A Copula-Based Modeling Approach for Future Projections. J. Appl. Meteorol. Climatol., 63(10), 1207-1225, 2024.

Asutosh, A., Tilmes, S., Bednarz, E. M., and Fadnavis, S. South Asian Summer Monsoon under stratospheric aerosol intervention. npj Clim. Atmos. Sci., 8(1), 3, 2025.

Bal, P. K., Pathak, R., Mishra, S. K., and Sahany, S. Effects of global warming and solar geoengineering on precipitation seasonality. Environ. Res. Lett. , 14(3), 034011, 2019.

Bala, G., Duffy, P., and Taylor, K. Impact of geoengineering schemes on the global hydrological cycle. PNAS, 105(22), 7664-7669, 2008.

Barnett, T. P., Adam, J. C., and Lettenmaier, D. P. Potential impacts of a warming climate on water availability in snow-dominated regions. Nature, 438(7066), 303-309, 2005.

Bednarz, E. M., Butler, A. H., Visioni, D., Zhang, Y., Kravitz, B., and MacMartin, D. G. Injection strategy–a driver of atmospheric circulation and ozone response to stratospheric aerosol geoengineering. Atmos. Chem. Phys., 23(21), 13665-13684, 2023.

https://doi.org/10.5194/egusphere-2026-3008
Preprint. Discussion started: 2 July 2026

1051 Bednarz, E. M., Butler, A. H., Haywood, J. M., Henry, M., Jones, A., Kravitz, B., Lee, W.
1052 R., MacMartin, D. G., Maycock, A. C., and Sekiya, T. Stratospheric ozone projections
1053 under sulfur-based stratospheric aerosol injection: Insights from the multi-model G6-
1054 1.5 K-SAI experiment. EGUsphere, 2026, 1-29, 2026.
1055 Berg, A., Sheffield, J., and Milly, P. C. Divergent surface and total soil moisture projections
1056 under global warming. Geophys. Res. Lett., 44(1), 236-244, 2017.
1057 Berghuijs, W., Woods, R., and Hrachowitz, M. A precipitation shift from snow towards
1058 rain leads to a decrease in streamflow. Nat. Clim. Change, 4(7), 583-586, 2014.
1059 Bhowmick, M., Mishra, S. K., Kravitz, B., Sahany, S., and Salunke, P. Response of the
1060 Indian summer monsoon to global warming, solar geoengineering and its termination.
1061 Sci. Rep., 11(1), 9791, 2021.
1062 Bland, J. M. and Altman, D. G. Multiple significance tests: the Bonferroni method. Bmj,
1063 310(6973), 170, 1995.
1064 Bonou, F., Da-Allada, C. Y., Baloitcha, E., Alamou, E., Biao, E. I., Zandagba, J., Obada,
1065 E., Pomalegni, Y., Irvine, P. J., and Tilmes, S. Stratospheric sulfate aerosols impacts
1066 on West African monsoon precipitation using GeoMIP models. Earth's Future, 11(11),
1067 2023.
1068 Bothe, O., Fraedrich, K., and Zhu, X. Precipitation climate of Central Asia and the large-
1069 scale atmospheric circulation. Theor. Appl. Climatol., 108(3), 345-354, 2012.
1070 Botsyun, S., Mutz, S. G., Ehlers, T. A., Koptev, A., Wang, X., Schmidt, B., Appel, E., and
1071 Scherer, D. E. Influence of large-scale atmospheric dynamics on precipitation
1072 seasonality of the Tibetan Plateau and Central Asia in cold and warm climates during
1073 the late cenozoic. J. Geophys. Res.: Atmos., 127(12), e2021JD035810, 2022.
1074 Chen, R., Duan, K., Shang, W., Shi, P., Meng, Y., and Zhang, Z. Increase in seasonal
1075 precipitation over the Tibetan Plateau in the 21st century projected using CMIP6
1076 models. Atmos. Res., 277, 106306, 2022.
1077 Chen, Y.-J., Hwang, Y.-T., and Lu, J. Robust increase in South Asian monsoon rainfall
1078 under warming driven by extratropical clouds and ocean. npj Clim. Atmos. Sci., 7(1),
1079 318, 2024.
1080 Cheng, L., Zhang, J., Wu, Y., Cheng, J., Yi, L., Zhang, Z., and Long, H. Westerly jet
1081 waviness modulates mid-latitude hydroclimate variability. Nat. Commun., 2025.
1082 Cheng, S., Guan, X., Huang, J., Ji, F., and Guo, R. Long-term trend and variability of soil
1083 moisture over East Asia. J. Geophys. Res.: Atmos., 120(17), 8658-8670, 2015.
1084 Cheng, W., MacMartin, D. G., Dagon, K., Kravitz, B., Tilmes, S., Richter, J. H., Mills, M.
1085 J., and Simpson, I. R. Soil moisture and other hydrological changes in a stratospheric
1086 aerosol geoengineering large ensemble. J. Geophys. Res.: Atmos., 124(23), 12773-
1087 12793, 2019.
1088 Clark, B., Xia, L., Robock, A., Tilmes, S., Richter, J. H., Visioni, D., and Rabin, S. S.
1089 Optimal climate intervention scenarios for crop production vary by nation. Nature
1090 Food, 4(10), 902-911, 2023.
1091 Cordak, A. S., Kooperman, G. J., Zarakas, C. M., Swann, A. L., and Koven, C. D. The role
1092 of leaf area changes within plant CO2 physiological impacts on the global hydrological
1093 cycle. Geophys. Res. Lett., 52(2), e2024GL110904, 2025.
1094 Crutzen, P. J. Albedo enhancement by stratospheric sulfur injections: a contribution to
1095 resolve a policy dilemma? Clim. Change, 77(3-4), 211, 2006.

https://doi.org/10.5194/egusphere-2026-3008
Preprint. Discussion started: 2 July 2026

Dagon, K. and Schrag, D. P. Regional climate variability under model simulations of solar geoengineering. J. Geophys. Res.: Atmos., 122(22), 12,106-112,121, 2017.
Dagon, K. and Schrag, D. P. Quantifying the effects of solar geoengineering on vegetation. Clim. Change, 153(1), 235-251, 2019.
Danabasoglu, G.: NCAR CESM2-WACCM model output prepared for CMIP6 GeoMIP G6sulfur, World Data Center for Climate (WDCC) at DKRZ [dataset], 2023.
Danabasoglu, G., Lamarque, J. F., Bacmeister, J., Bailey, D., DuVivier, A., Edwards, J., Emmons, L., Fasullo, J., Garcia, R., and Gettelman, A. The community earth system model version 2 (CESM2). J. Adv. Model. Earth Syst. , 12(2), e2019MS001916, 2020.
Deng, H., Pepin, N., and Chen, Y. Changes of snowfall under warming in the Tibetan Plateau. J. Geophys. Res.: Atmos., 122(14), 7323-7341, 2017.
Dong, X., Liu, Y., Yan, X., Wang, Y., Tan, Z., Luo, M., Li, D., Wang, Y., and Tang, S. Compound impacts of South Asian summer monsoon and westerlies on summer precipitation over Tibetan Plateau. Clim. Dyn., 62(5), 3067-3087, 2024.
Duffey, A. and Irvine, P. J. Accounting for transience in the baseline climate state changes the surface climate response attributed to stratospheric aerosol injection. Environ. Res.: Clim., 3(4), 041008, 2024.
Effiong, U. and Neitzel, R. L. Assessing the direct occupational and public health impacts of solar radiation management with stratospheric aerosols. Environ. Health, 15, 1-9, 2016.
Eyring, V., Bony, S., Meehl, G. A., Senior, C. A., Stevens, B., Stouffer, R. J., and Taylor, K. E. Overview of the Coupled Model Intercomparison Project Phase 6 (CMIP6) experimental design and organization. Geosci. Model Dev., 9(5), 1937-1958, 2016.
Fallah, B., Didovets, I., Rostami, M., and Hamidi, M. Climate change impacts on Central Asia: Trends, extremes and future projections. Int. J. Climatol., 44(10), 3191-3213, 2024.
Feng, S., Hu, Q., Huang, W., Ho, C.-H., Li, R., and Tang, Z. Projected climate regime shift under future global warming from multi-model, multi-scenario CMIP5 simulations. Global Planet. Change, 112, 41-52, 2014.
Feng, Z.-Q., Tan, M. L., Juneng, L., Tye, M. R., Xia, L.-L., and Zhang, F. Effects of solar radiation modification on precipitation extremes in Southeast Asia: Insights from the GeoMIP G6 experiments. Adv. Clim. Change Res., 16(3), 591-605, 2025.
Fernández, A., Manquehual-Cheuque, F., and Somos-Valenzuela, M. Impact of Solar Radiation Management on Andean glacier-wide surface mass balance. npj Clim. Atmos. Sci., 7(1), 257, 2024.
Fisher, R. A., Wieder, W. R., Sanderson, B. M., Koven, C. D., Oleson, K. W., Xu, C., Fisher, J. B., Shi, M., Walker, A. P., and Lawrence, D. M. Parametric controls on vegetation responses to biogeochemical forcing in the CLM5. J. Adv. Model. Earth Syst. , 11(9), 2879-2895, 2019.
Gay, B. A., Mandrake, L., Miner, K. R., and Miller, C. E. Assessing the impacts of mitigation and geoengineering intervention scenarios on Earth Syst. Dyn. and climatological variability with multimodal simulations. Sci. Rep., 15(1), 8158, 2025.
Gettelman, A., Hannay, C., Bacmeister, J. T., Neale, R. B., Pendergrass, A., Danabasoglu, G., Lamarque, J. F., Fasullo, J., Bailey, D., and Lawrence, D. High climate sensitivity

https://doi.org/10.5194/egusphere-2026-3008
Preprint. Discussion started: 2 July 2026

in the Community Earth System Model version 2 (CESM2). Geophys. Res. Lett., 46(14), 8329-8337, 2019.
Guan, Y., Zhang, X., Zheng, F., and Wang, B. Trends and variability of daily temperature extremes during 1960–2012 in the Yangtze River Basin, China. Global Planet. Change, 124, 79-94, 2015.
Guan, Y., Zheng, F., Zhang, X., and Wang, B. Trends and variability of daily precipitation and extremes during 1960–2012 in the Yangtze River Basin, China. Int. J. Climatol., 37(3), 1282-1298, 2017.
Guo, H., Bao, A., Chen, T., Zheng, G., Wang, Y., Jiang, L., and De Maeyer, P. Assessment of CMIP6 in simulating precipitation over arid Central Asia. Atmos. Res., 252, 105451, 2021.
Haile, G. G., Tang, Q., Li, W., Liu, X., and Zhang, X. Drought: Progress in broadening its understanding. Wiley Interdisciplinary Reviews: Water, 7(2), e1407, 2020.
Held, I. M. and Soden, B. J. Robust responses of the hydrological cycle to global warming. J. clim., 19(21), 5686-5699, 2006.
Henry, M., Bednarz, E. M., and Haywood, J. How does the latitude of stratospheric aerosol injection affect the climate in UKESM1? Atmos. Chem. Phys., 24(23), 13253-13268, 2024.
Hermans, K., Djanibekov, N., Abdullaev, I., Abduvalieva, N., Assubayeva, A., Blondin, S., Bobojonov, I., Conrad, C., Herzfeld, T., and Kansiime, J. Future research directions for understanding the interconnections between climate change, water scarcity, and mobility in rural Central Asia. Clim. Dev., 17(7), 638-647, 2025.
Hu, Y., Yu, H., Kang, S., Xu, M., Chen, S., Yang, J., Chen, X., and Li, J. Reduced aerosol transport from South Asia to the Tibetan Plateau following the January 2021 sudden stratospheric warming event. Commun. Earth Environ., 5(1), 706, 2024.
Hua, L., Zhao, T., and Zhong, L. Future changes in drought over Central Asia under CMIP6 forcing scenarios. J. Hydrol.: Reg. Stud., 43, 101191, 2022.
Huang, J., Ji, M., Xie, Y., Wang, S., He, Y., and Ran, J. Global semi-arid climate change over last 60 years. Clim. Dyn., 46(3), 1131-1150, 2016.
Huang, W., Duan, W., and Chen, Y. Rapidly declining surface and terrestrial water resources in Central Asia driven by socio-economic and climatic changes. Sci. Total Environ., 784, 147193, 2021.
Hussain, A., Khan, M. A., and Shoaib, M. Impacts of Solar Geoengineering on Malaria Transmission in South Asia. Authorea Preprints, 2024a.
Hussain, A., Khan, M. A., and Sipra, H. Impacts of Solar Geoengineering on Projected Climate of South Asia. Int. J. Climatol., 45(2), e8695, 2025a.
Hussain, A., Hussain, I., Rezaei, A., Ullah, W., Lu, M., Zhou, J., and Guan, Y. Increasing monsoon precipitation extremes in relation to large-scale climatic patterns in Pakistan. Atmos. Res., 309, 107592, 2024b.
Hussain, A., Cao, J., Hussain, I., Begum, S., Akhtar, M., Wu, X., Guan, Y., and Zhou, J. Observed trends and variability of temperature and precipitation and their global teleconnections in the Upper Indus Basin, Hindukush-Karakoram-Himalaya. Atmosphere, 12(8), 973, 2021.
Hussain, A., Liu, H., Cao, J., Yang, H., Rezaei, A., Wang, P., Luo, Q., Zhou, M., and Liang, Z. Recent increase in soil moisture levels concerning climate variability in the karst

https://doi.org/10.5194/egusphere-2026-3008
Preprint. Discussion started: 2 July 2026

region of southwest China using wavelet coherence and multi-linear regression. Gondwana Res., 2025b.

Hussain, A., Cao, J., Abbas, H., Hussain, I., Zhou, J., Yang, H., Rezaei, A., Luo, Q., Ullah, W., and Liang, Z. Characterizing the local and global climatic factors associated with vegetation dynamics in the karst region of southwest China. J. Hydrol., 643, 132018, 2024c.

Huynh, H. N. and McNeill, V. F. The potential environmental and climate impacts of stratospheric aerosol injection: A review. Environ. Sci.: Atmos, 4(2), 114-143, 2024.

Ibatullin, S., Yasinskiy, V., and Mironenkov, A. The impact of climate change on water resources in Central Asia. Eurasian Development Bank, Sector Report(6), 2009.

Immerzeel, W. W., Van Beek, L. P., and Bierkens, M. F. Climate change will affect the Asian water towers. science, 328(5984), 1382-1385, 2010.

IPCC Global Warming of 1.5°C.An IPCC Special Report on the impacts of global warming of 1.5°C above pre-industrial levels and related global greenhouse gas emission pathways, in the context of strengthening the global response to the threat of climate change, sustainable development, and efforts to eradicate poverty [Masson-Delmotte, V., P. Zhai, H.-O. Pörtner, D. Roberts, J. Skea, P.R. Shukla, A. Pirani, W. Moufouma-Okia, C. Péan, R. Pidcock, S. Connors, J.B.R. Matthews, Y. Chen, X. Zhou, M.I. Gomis, E. Lonnoy, T. Maycock, M. Tignor, and T. Waterfield (eds.)]. In Press., 2018.

IPCC: Summary for policymakers. In: Climate Change 2021: The Physical ScienceBasis. Contribution of Working Group I to the Sixth Assessment Report of theIntergovernmental Panel on Climate Change, 2391, 2021.

Irvine, P. J. and Keith, D. W. Halving warming with stratospheric aerosol geoengineering moderates policy-relevant climate hazards. Environ. Res. Lett. , 15(4), 044011, 2020.

Iturbide, M., Gutiérrez, J. M., Alves, L. M., Bedia, J., Cerezo-Mota, R., Cimadevilla, E., Cofiño, A. S., Di Luca, A., Faria, S. H., and Gorodetskaya, I. V. An update of IPCC climate reference regions for subcontinental analysis of climate model data: definition and aggregated datasets. Earth Syst. Sci. Data, 12(4), 2959-2970, 2020.

Jiang, J. and Zhou, T.: Agricultural drought over water-scarce Central Asia aggravated by internal climate variability. Nat Geosci 16: 154–161, 2023.

Jiang, J., Zhou, T., Chen, X., and Zhang, L. Future changes in precipitation over Central Asia based on CMIP6 projections. Environ. Res. Lett. , 15(5), 054009, 2020.

Jiang, T., Jia, G., Yu, X., Zhang, T., and Feng, Y. Hydrologic response to extreme climate change in the Qinghai Lake Basin. Ecol. Ind., 178, 114048, 2025.

Jin, Z., Xu, K., Ge, F., Wang, W., and Lin, Z. Boost to early spring compound heatwaves over South Asia from anomalous Tibetan Plateau atmospheric heat source. Atmos. Res., 305, 107449, 2024.

Jones, A., Haywood, J. M., Jones, A. C., Tilmes, S., Kravitz, B., and Robock, A. North Atlantic Oscillation response in GeoMIP experiments G6solar and G6sulfur: why detailed modelling is needed for understanding regional implications of solar radiation management. Atmos. Chem. Phys., 21(2), 1287-1304, 2021.

Jones, A., Haywood, J. M., Scaife, A. A., Boucher, O., Henry, M., Kravitz, B., Lurton, T., Nabat, P., Niemeier, U., and Séférian, R. The impact of stratospheric aerosol intervention on the North Atlantic and quasi-biennial oscillations in the geoengineering model intercomparison project (GeoMIP) G6sulfur experiment. Atmos. Chem. Phys., 22(5), 2999-3016, 2022.

https://doi.org/10.5194/egusphere-2026-3008
Preprint. Discussion started: 2 July 2026

Jones, A. C., Hawcroft, M. K., Haywood, J. M., Jones, A., Guo, X., and Moore, J. C. Regional climate impacts of stabilizing global warming at 1.5 K using solar geoengineering. Earth's Future, 6(2), 230-251, 2018.

Keeble, J., Hassler, B., Banerjee, A., Checa-Garcia, R., Chiodo, G., Davis, S., Eyring, V., Griffiths, P. T., Morgenstern, O., and Nowack, P. Evaluating stratospheric ozone and water vapor changes in CMIP6 models from 1850–2100. Atmos. Chem. Phys. Discussions, 2020, 1-68, 2020.

Khan, F. Water availability and response of Tarbela Reservoir under the changing climate in the Upper Indus Basin, Pakistan. Sci. Rep., 12(1), 15865, 2022.

Kim, J.-B. and Bae, D.-H. Intensification characteristics of hydroclimatic extremes in the Asia monsoon region under 1.5 and 2.0 C of global warming. Hydrol. Earth Syst. Sci. Discuss., 2020, 1-30, 2020.

Kravitz, B., Robock, A., Boucher, O., Schmidt, H., Taylor, K. E., Stenchikov, G., and Schulz, M. The geoengineering model intercomparison project (GeoMIP). Atmos. Sci. Lett., 12(2), 162-167, 2011.

Kravitz, B., Caldeira, K., Boucher, O., Robock, A., Rasch, P. J., Alterskjaer, K., Karam, D. B., Cole, J. N., Curry, C. L., and Haywood, J. M. Climate model response from the geoengineering model intercomparison project (GeoMIP). J. Geophys. Res.: Atmos., 118(15), 8320-8332, 2013a.

Kravitz, B., Rasch, P. J., Forster, P. M., Andrews, T., Cole, J. N., Irvine, P. J., Ji, D., Kristjánsson, J. E., Moore, J. C., and Muri, H. An energetic perspective on hydrological cycle changes in the Geoengineering Model Intercomparison Project. J. Geophys. Res.: Atmos., 118(23), 13,087-013,102, 2013b.

Laakso, A., Visioni, D., Niemeier, U., Tilmes, S., and Kokkola, H. Dependency of the impacts of geoengineering on the stratospheric sulfur injection strategy–Part 2: How changes in the hydrological cycle depend on the injection rate and model used. Earth Syst. Dyn., 15(2), 405-427, 2024.

Lang, Y., Zhang, J., Zhao, J., Gong, Y., Han, T., Deng, X., and Liu, Y. Mechanisms and quantification: How anthropogenic aerosols weaken the East Asian summer monsoon. npj Clim. Atmos. Sci., 8(1), 13, 2025.

Lawrence, D. M., Fisher, R. A., Koven, C. D., Oleson, K. W., Swenson, S. C., Bonan, G., Collier, N., Ghimire, B., Van Kampenhout, L., and Kennedy, D. The Community Land Model version 5: Description of new features, benchmarking, and impact of forcing uncertainty. J. Adv. Model. Earth Syst. , 11(12), 4245-4287, 2019.

Lee, W. R., Visioni, D., Wagman, B. M., Wentland, C. R., Kravitz, B., Watanabe, S., Sekiya, T., Jones, A., Haywood, J., and Henry, M. G6-1.5 K-SAI and G6sulfur: changes in impacts and uncertainty depending on stratospheric aerosol injection strategy in the Geoengineering Model Intercomparison Project. EGUsphere, 2025, 1-33, 2025.

Li, C., Hao, J., Zhang, G., Wang, Y., Fang, H., Hou, W., and Cui, P. Extreme snowfall variations in the Southeastern Tibetan Plateau under warming climate. Atmos. Res., 311, 107690, 2024.

Li, D., Lu, X., Walling, D. E., Zhang, T., Steiner, J. F., Wasson, R. J., Harrison, S., Nepal, S., Nie, Y., and Immerzeel, W. W. High Mountain Asia hydropower systems threatened by climate-driven landscape instability. Nat. Geosci., 15(7), 520-530, 2022a.

https://doi.org/10.5194/egusphere-2026-3008
Preprint. Discussion started: 2 July 2026

Li, R., Feng, Q., and Cui, Y. Precipitation recycling impacts on runoff in arid regions of China and Mongolia: a machine learning approach. Hydrol. Sci. J., 70(5), 730-749, 2025.

Li, X., Liu, X., Zhao, K., Zhang, X., and Li, L. Change in the potential snowfall phenology: past, present, and future in the Chinese Tianshan mountainous region, Central Asia. The Cryosphere, 17(6), 2437-2453, 2023.

Li, X., Long, D., Scanlon, B. R., Mann, M. E., Li, X., Tian, F., Sun, Z., and Wang, G. Climate change threatens terrestrial water storage over the Tibetan Plateau. Nat. Clim. Change, 12(9), 801-807, 2022b.

Liang, Z., Rao, J., Guo, D., and Lu, Q. Simulation and projection of the sudden stratospheric warming events in different scenarios by CESM2-WACCM. Clim. Dyn., 59(11), 3741-3761, 2022.

Lin, X., Huang, S., Li, J., Huang, Q., Shi, H., She, D., Leng, G., Wei, X., Guo, W., and Liu, Y. Feedback dynamics between precipitation, temperature, and soil moisture in China and their possible driving mechanisms under a changing environment. Atmos. Res., 106983, 2023.

Lindeman, R. H., Merenda, P. F., and Gold, R. Z.: Introduction to bivariate and multivariate analysis (No. 04, QA278, L553), Scott, Foresman Glenview, IL, Uniq ID: 5310754, 1980.

Liu, Y., Li, Z., Chen, Y., Jin, L., Li, F., Wang, X., Long, Y., Liu, C., and Kayumba, P. M. Global greening drives significant soil moisture loss. Commun. Earth Environ., 6(1), 600, 2025.

Liu, Z., Lang, X., and Jiang, D. Impact of stratospheric aerosol injection geoengineering on the summer climate over East Asia. J. Geophys. Res.: Atmos., 126(22), e2021JD035049, 2021.

Liu, Z., Lang, X., and Jiang, D. Stratospheric aerosol injection geoengineering would mitigate greenhouse gas-induced drying and affect global drought patterns. J. Geophys. Res.: Atmos., 129(3), e2023JD039988, 2024.

Luo, H., Wang, Z., He, C., Chen, D., and Yang, S. Future changes in South Asian summer monsoon circulation under global warming: role of the Tibetan Plateau latent heating. npj Clim. Atmos. Sci., 7(1), 103, 2024.

Lutz, A., Immerzeel, W., Shrestha, A., and Bierkens, M. Consistent increase in High Asia's runoff due to increasing glacier melt and precipitation. Nat. Clim. Change, 4(7), 587-592, 2014.

Ma, X., Zhu, J., Yan, W., and Zhao, C. Projections of desertification trends in Central Asia under global warming scenarios. Sci. Total Environ., 781, 146777, 2021.

MacMartin, D. G., Kravitz, B., Tilmes, S., Richter, J. H., Mills, M. J., Lamarque, J. F., Tribbia, J. J., and Vitt, F. The climate response to stratospheric aerosol geoengineering can be tailored using multiple injection locations. J. Geophys. Res.: Atmos., 122(23), 12,574-512,590, 2017.

Magara, G., Haque, M., Okrah, A., Nyasulu, M., Yeboah, E., Ebaju, G. K., Akimana, D., Hasan, T., and Mostahidul Hasan, S. Evaluating CMIP6 models for CO2 and CH4 concentrations across Africa: performance, biases, and implications for climate predictions. Clim. Dyn., 63(5), 1-18, 2025.

Meehl, G. A., Arblaster, J. M., Bates, S., Richter, J. H., Tebaldi, C., Gettelman, A., Medeiros, B., Bacmeister, J., DeRepentigny, P., and Rosenbloom, N. Characteristics

https://doi.org/10.5194/egusphere-2026-3008
Preprint. Discussion started: 2 July 2026

of future warmer base states in CESM2. Earth Space Sci., 7(9), e2020EA001296, 2020.
Meng, Y., Duan, K., Shi, P., Shang, W., Li, S., Cheng, Y., Xing, L., Chen, R., and He, J. Sensitive temperature changes on the Tibetan Plateau in response to global warming. Atmos. Res., 294, 106948, 2023.
Miao, L., Li, S., Zhang, F., Chen, T., Shan, Y., and Zhang, Y. Future drought in the dry lands of Asia under the 1.5 and 2.0 C warming scenarios. Earth's Future, 8(6), e2019EF001337, 2020.
Milly, P. C., Betancourt, J., Falkenmark, M., Hirsch, R. M., Kundzewicz, Z. W., Lettenmaier, D. P., and Stouffer, R. J. Stationarity is dead: Whither water management? Science, 319(5863), 573-574, 2008.
Mmame, B., Sunitha, P., Samatha, K., Rao, S., Satish, P., Amasarao, A., and Sekhar, K. C. Assessment of CMIP6 model performance in simulating atmospheric aerosol and precipitation over Africa. Adv. Space Res., 72(8), 3096-3108, 2023.
Moore, J. C., Yue, C., Chen, Y., Jevrejeva, S., Visioni, D., Uotila, P., and Zhao, L. Multi-model simulation of solar geoengineering indicates avoidable destabilization of the West Antarctic ice sheet. Earth's Future, 12(6), e2024EF004424, 2024.
Naumann, G., Alfieri, L., Wyser, K., Mentaschi, L., Betts, R. A., Carrao, H., Spinoni, J., Vogt, J., and Feyen, L. Global changes in drought conditions under different levels of warming. Geophys. Res. Lett., 45(7), 3285-3296, 2018.
Nawaz, F., Wang, T., and Hussain, A. Spatiotemporal Runoff Analysis and Associated Influencing Factors in Chitral Basin, Pakistan. Water, 15(12), 2175, 2023.
Nie, Y., Pritchard, H. D., Liu, Q., Hennig, T., Wang, W., Wang, X., Liu, S., Nepal, S., Samyn, D., and Hewitt, K. Glacial change and hydrological implications in the Himalaya and Karakoram. Nat. Rev. Earth Environ., 2(2), 91-106, 2021.
Niemeier, U. and Schmidt, H. Changing transport processes in the stratosphere by radiative heating of sulfate aerosols. Atmos. Chem. Phys., 17(24), 14871-14886, 2017.
O'Neill, B. C., Tebaldi, C., van Vuuren, D. P., Eyring, V., Friedlingstein, P., Hurtt, G., Knutti, R., Kriegler, E., Lamarque, J.-F., and Lowe, J. The Scenario Model Intercomparison Project (ScenarioMIP) for CMIP6. 2016.
Park, C.-E., Jeong, S.-J., Joshi, M., Osborn, T. J., Ho, C.-H., Piao, S., Chen, D., Liu, J., Yang, H., and Park, H. Keeping global warming within 1.5 C constrains emergence of aridification. Nat. Clim. Change, 8(1), 70-74, 2018.
Patel, T. D., Odoulami, R. C., Pinto, I., Egbebiyi, T. S., Lennard, C., Abiodun, B. J., and New, M. Potential impact of stratospheric aerosol geoengineering on projected temperature and precipitation extremes in South Africa. Environ. Res.: Clim., 2(3), 035004, 2023.
Petrie, R., Denvil, S., Ames, S., Levavasseur, G., Fiore, S., Allen, C., Antonio, F., Berger, K., Bretonnière, P.-A., and Cinquini, L. Coordinating an operational data distribution network for CMIP6 data. Geosci. Model Dev. Discussions, 2020, 1-22, 2020.
Pope, F. D., Braesicke, P., Grainger, R., Kalberer, M., Watson, I., Davidson, P., and Cox, R. Stratospheric aerosol particles and solar-radiation management. Nat. Clim. Change, 2(10), 713-719, 2012.
Price, J., Warren, R., Forstenhäusler, N., Wallace, C., Jenkins, R., Osborn, T. J., and Van Vuuren, D. Quantification of meteorological drought risks between 1.5 C and 4 C of global warming in six countries. Clim. Change, 174(1), 12, 2022.

https://doi.org/10.5194/egusphere-2026-3008
Preprint. Discussion started: 2 July 2026

Qie, K., Tian, W., Bian, J., Xie, F., and Li, D. Weakened Asian summer monsoon anticyclone related to increased anthropogenic aerosol emissions in recent decades. npj Clim. Atmos. Sci., 8(1), 140, 2025.

Rebi, A., Hussain, A., Hussain, I., Cao, J., Ullah, W., Abbas, H., Ullah, S., and Zhou, J. Spatiotemporal Precipitation Trends and Associated Large-Scale Teleconnections in Northern Pakistan. Atmosphere, 14(5), 871, 2023.

Reboita, M. S., Crespo, N. M., Ribeiro, J. G. M., and da Rocha, R. P. South Atlantic subtropical anticyclone responses to stratospheric aerosol injection. Environ. Res.: Clim., 4(1), 015003, 2025.

Reboita, M. S., Ribeiro, J. G. M., Crespo, N. M., da Rocha, R. P., Odoulami, R. C., Sawadogo, W., and Moore, J. Response of the Southern Hemisphere extratropical cyclone climatology to climate intervention with stratospheric aerosol injection. Environ. Res.: Clim., 3(3), 035006, 2024.

Ren, Y., Yu, H., Huang, J., Peng, M., and Zhou, J. The projected response of the water cycle to global warming over drylands in East Asia. Earth's Future, 12(4), e2023EF004008, 2024.

Rezaei, A., Karami, K., Tilmes, S., and Moore, J. C. Changes in global teleconnection patterns under global warming and stratospheric aerosol intervention scenarios. Atmos. Chem. Phys., 23(10), 5835-5850, 2023.

Rezaei, A., Karami, K., Tilmes, S., and Moore, J. C. Future water storage changes over the Mediterranean, Middle East, and North Africa in response to global warming and stratospheric aerosol intervention. Earth Syst. Dyn., 15(1), 91-108, 2024.

Rezaei, A., Moore, J., Tilmes, S., and Karami, K. Regional and seasonal hydrological changes with and without Stratospheric Aerosol Intervention under High Greenhouse Gas climates. J. Geophys. Res.: Atmos., 130(12), e2025JD044163, 2025a.

Rezaei, A., Moore, J., Tilmes, S., Visioni, D., and Hussain, A. Multi-model future world aridity and groundwater recharge changes with and without stratospheric aerosol intervention under high warming scenario. Geophys. Res. Lett., 52(17), e2025GL117234, 2025b.

Richter, J. H., Visioni, D., MacMartin, D. G., Bailey, D. A., Rosenbloom, N., Dobbins, B., Lee, W. R., Tye, M., and Lamarque, J.-F. Assessing Responses and Impacts of Solar climate intervention on the Earth system with stratospheric aerosol injection (ARISE-SAI): protocol and initial results from the first simulations. Geosci. Model Dev., 15(22), 8221-8243, 2022.

Ricke, K., Wan, J. S., Saenger, M., and Lutsko, N. J. Hydrological consequences of solar geoengineering. Annual review of earth and planetary sciences, 51(1), 447-470, 2023.

Robock, A., Oman, L., and Stenchikov, G. L. Regional climate responses to geoengineering with tropical and Arctic SO2 injections. J. Geophys. Res.: Atmos., 113(D16), 2008.

Samaniego, L., Thober, S., Kumar, R., Wanders, N., Rakovec, O., Pan, M., Zink, M., Sheffield, J., Wood, E. F., and Marx, A. Anthropogenic warming exacerbates European soil moisture droughts. Nat. Clim. Change, 8(5), 421-426, 2018.

Savitskiy, A. G., Schlüter, M., Taryannikova, R. V., Agaltseva, N. A., and Chub, V. E.: Current and future impacts of climate change on river runoff in the Central Asian river basins, in: Adaptive and Integrated Water Management: Coping with Complexity and Uncertainty, Springer, 323-339, 2008.

https://doi.org/10.5194/egusphere-2026-3008
Preprint. Discussion started: 2 July 2026

Schiemann, R., Lüthi, D., Vidale, P. L., and Schär, C. The precipitation climate of Central Asia—intercomparison of observational and numerical data sources in a remote semiarid region. Int. J. Climatol., 28(3), 295-314, 2008.

Schiferl, L. D., Heald, C. L., and Kelly, D. Resource and physiological constraints on global crop production enhancements from atmospheric particulate matter and nitrogen deposition. Biogeosciences, 15(14), 4301-4315, 2018.

Simpkins, G. A drier future for South Asia. Nat. Rev. Earth Environ., 1(11), 557-557, 2020.

Simpson, I., Tilmes, S., Richter, J., Kravitz, B., MacMartin, D., Mills, M. J., Fasullo, J., and Pendergrass, A. G. The regional hydroclimate response to stratospheric sulfate geoengineering and the role of stratospheric heating. J. Geophys. Res.: Atmos., 124(23), 12587-12616, 2019.

Simpson, I. R., Bacmeister, J., Neale, R. B., Hannay, C., Gettelman, A., Garcia, R. R., Lauritzen, P. H., Marsh, D. R., Mills, M. J., and Medeiros, B. An evaluation of the large-scale atmospheric circulation and its variability in CESM2 and other CMIP models. J. Geophys. Res.: Atmos., 125(13), e2020JD032835, 2020.

Stevenson, S., Coats, S., Touma, D., Cole, J., Lehner, F., Fasullo, J., and Otto-Bliesner, B. Twenty-first century hydroclimate: A continually changing baseline, with more frequent extremes. PNAS, 119(12), e2108124119, 2022.

Tan, M. L., Tew, Y. L., Liew, J., Bala, G., Tye, M. R., Chang, C. K., and Muhamad, N. Assessment of solar geoengineering impact on precipitation and temperature extremes in the Muda River Basin, Malaysia using CMIP6 SSP and GeoMIP6 G6 simulations. Sci. Total Environ., 948, 174817, 2024.

Tilmes, S. GeoMIP SSP5 run data. Research Data Archive at the National Center for Atmos. Res., Computational and In-formation Systems Laboratory., https://doi.org/10.5065/3WEZ-DD73, 2024.

Tilmes, S., MacMartin, D. G., Lenaerts, J. T., Van Kampenhout, L., Muntjewerf, L., Xia, L., Harrison, C. S., Krumhardt, K. M., Mills, M. J., and Kravitz, B. Reaching 1.5 and 2.0◦ C global surface temperature targets using stratospheric aerosol geoengineering. Earth Syst. Dyn., 11(3), 579-601, 2020.

Tilmes, S., Richter, J. H., Kravitz, B., MacMartin, D. G., Mills, M. J., Simpson, I. R., Glanville, A. S., Fasullo, J. T., Phillips, A. S., and Lamarque, J.-F. CESM1 (WACCM) stratospheric aerosol geoengineering large ensemble project. Bull. Am. Meteorol. Soc., 99(11), 2361-2371, 2018.

Ullah, I., Zeng, X. M., Mukherjee, S., Aadhar, S., Mishra, A. K., Syed, S., Ayugi, B. O., Iyakaremye, V., and Lv, H. Future amplification of multivariate risk of compound drought and heatwave events on South Asian population. Earth's Future, 11(12), e2023EF003688, 2023a.

Ullah, S., You, Q., Ullah, W., Sachindra, D., Ali, A., Bhatti, A. S., and Ali, G. Climate change will exacerbate population exposure to future heat waves in the China-Pakistan economic corridor. Weather Clim. Extremes, 40, 100570, 2023b.

Ullah, S., You, Q., Chen, D., Sachindra, D., AghaKouchak, A., Kang, S., Li, M., Zhai, P., and Ullah, W. Future population exposure to daytime and nighttime heat waves in South Asia. Earth's Future, 10(5), e2021EF002511, 2022.

Ullah, W., Karim, A., Ullah, S., Rehman, A.-U., Bibi, T., Wang, G., Ullah, S., Bhatti, A. S., Ali, G., and Abbas, A. An increasing trend in daily monsoon precipitation extreme

https://doi.org/10.5194/egusphere-2026-3008
Preprint. Discussion started: 2 July 2026

indices over Pakistan and its relationship with atmospheric circulations. Front. Environ. Sci., 11, 1228817, 2023c.
Vicente-Serrano, S. M., Quiring, S. M., Peña-Gallardo, M., Yuan, S., and Domínguez-Castro, F. A review of environmental droughts: Increased risk under global warming? Earth-Science Reviews, 201, 102953, 2020.
Vicente-Serrano, S. M., McVicar, T. R., Miralles, D. G., Yang, Y., and Tomas-Burguera, M. Unraveling the influence of atmospheric evaporative demand on drought and its response to climate change. Wiley Interdisciplinary Reviews: Climate Change, 11(2), e632, 2020.
Visioni, D., Bednarz, E., MacMartin, D., Kravitz, B., and Goddard, P. B. The choice of baseline period influences the assessments of the outcomes of stratospheric aerosol injection. Earth's Future, 11(8), e2023EF003851, 2023.
Visioni, D., MacMartin, D. G., Kravitz, B., Lee, W., Simpson, I. R., and Richter, J. H. Reduced poleward transport due to stratospheric heating under stratospheric aerosols geoengineering. Geophys. Res. Lett., 47(17), e2020GL089470, 2020a.
Visioni, D., MacMartin, D. G., Kravitz, B., Richter, J. H., Tilmes, S., and Mills, M. J. Seasonally modulated stratospheric aerosol geoengineering alters the climate outcomes. Geophys. Res. Lett., 47(12), e2020GL088337, 2020b.
Visioni, D., Jones, A., Haywood, J., Séférian, R., Nabat, P., Boucher, O., Bednarz, E. M., and Niemeier, U. Stratospheric ozone response to sulfate aerosol and solar dimming climate interventions based on the G6 Geoengineering Model Intercomparison Project (GeoMIP) simulations. Atmos. Chem. Phys., 22(7), 4557-4579, 2022.
Visioni, D., MacMartin, D. G., Kravitz, B., Boucher, O., Jones, A., Lurton, T., Martine, M., Mills, M. J., Nabat, P., and Niemeier, U. Identifying the sources of uncertainty in climate model simulations of solar radiation modification with the G6sulfur and G6solar Geoengineering Model Intercomparison Project (GeoMIP) simulations. Atmos. Chem. Phys., 21(13), 10039-10063, 2021.
Visioni, D., Robock, A., Haywood, J., Henry, M., Tilmes, S., MacMartin, D. G., Kravitz, B., Doherty, S. J., Moore, J., and Lennard, C. G6-1.5 K-SAI: a new Geoengineering Model Intercomparison Project (GeoMIP) experiment integrating recent advances in solar radiation modification studies. Geosci. Model Dev., 17(7), 2583-2596, 2024.
Voumik, L. C., Mimi, M. B., and Raihan, A. Nexus between urbanization, industrialization, natural resources rent, and anthropogenic carbon emissions in South Asia: CS-ARDL approach. Anthropocene Sci., 2(1), 48-61, 2023.
Wang, B., Bao, Q., Hoskins, B., Wu, G., and Liu, Y. Tibetan Plateau warming and precipitation changes in East Asia. Geophys. Res. Lett., 35(14), 2008.
Wang, J., Xu, B., Li, Z., Nasir, J., Farhan, S. B., Wang, M., Xie, Y., Yang, S., Cauquoin, A., and Hussain, A. The interpretation of Karakoram anomaly by high Karakoram ice core record. J. Geophys. Res.: Atmos., 130(1), e2023JD040235, 2025.
Wang, Y., Yang, K., Huang, W., Qiu, T., and Wang, B. Dominant contribution of South Asia monsoon to external moisture for extreme precipitation events in northern Tibetan Plateau. Remote Sensing, 15(3), 735, 2023a.
Wang, Y., Wang, S., Wang, L., Guo, X., Zhou, J., Chai, C., Xu, J., Li, X., Fan, M., and Wang, S. Temporal and spatial changes in hydrological wet extremes of the largest river basin on the Tibetan Plateau. Environ. Res. Lett. , 18(10), 104006, 2023b.

https://doi.org/10.5194/egusphere-2026-3008
Preprint. Discussion started: 2 July 2026

Wei, W., Zou, S., Duan, W., Chen, Y., Li, S., and Zhou, Y. Spatiotemporal variability in extreme precipitation and associated large-scale climate mechanisms in Central Asia from 1950 to 2019. J. Hydrol., 620, 129417, 2023.

Weisenstein, D. K., Keith, D. W., and Dykema, J. Solar geoengineering using solid aerosol in the stratosphere. Atmos. Chem. Phys., 15(20), 11835-11859, 2015.

Wells, A. F., Henry, M., Bednarz, E. M., MacMartin, D. G., Jones, A., Dalvi, M., and Haywood, J. M. Identifying climate impacts from different stratospheric aerosol injection strategies in UKESM1. Earth's Future, 12(3), e2023EF004358, 2024.

Wheeler, L., Wagman, B., Smith, W., Davies, P., Cook, B., Brunell, S., Glen, A., Hackenburg, D., Lien, J., and Shand, L. Design and simulation of a logistically constrained high-latitude, low-altitude stratospheric aerosol injection scenario in the Energy Exascale Earth System Model (E3SM). Environ. Res. Lett., 20(4), 044011, 2025.

Wu, X., Tang, W., Chen, F., Wang, S., Bakhtiyorov, Z., Liu, Y., and Guan, Y. Attribution and risk projections of hydrological drought over water-scarce Central Asia. Earth's Future, 13(1), e2024EF005243, 2025.

Xia, J., Ning, L., Wang, Q., Chen, J., Wan, L., and Hong, S. Vulnerability of and risk to water resources in arid and semi-arid regions of West China under a scenario of climate change. Clim. Change, 144(3), 549-563, 2017a.

Xia, L., Nowack, P. J., Tilmes, S., and Robock, A. Impacts of stratospheric sulfate geoengineering on tropospheric ozone. Atmos. Chem. Phys., 17(19), 11913-11928, 2017b.

Xu, Y., Zhou, B.-T., Wu, J., Han, Z.-Y., Zhang, Y.-X., and Wu, J. Asian climate change under 1.5–4 C warming targets. Adv. Clim. Change Res., 8(2), 99-107, 2017.

Yang, K., Chen, W., Ren, G., and Zhang, R. Spatial patterns and drivers of elevation dependency of extreme temperature changes on the Tibetan Plateau. Clim. Dyn., 63(6), 247, 2025.

Yang, T., Li, Q., Chen, X., De Maeyer, P., Yan, X., Liu, Y., Zhao, T., and Li, L. Spatiotemporal variability of the precipitation concentration and diversity in Central Asia. Atmos. Res., 241, 104954, 2020.

Yao, J.-Q., Chen, J., Zhang, T.-W., Dilinuer, T., and Mao, W.-Y. Stationarity in the variability of arid precipitation: A case study of arid Central Asia. Adv. Clim. Change Res., 12(2), 172-186, 2021.

You, N., Meng, J., and Zhu, L. Sensitivity and resilience of ecosystems to climate variability in the semi-arid to hyper-arid areas of Northern China: a case study in the Heihe River Basin. Ecol. Res., 33(1), 161-174, 2018.

Yu, W., Liu, Y., Yang, X.-Q., Wu, G., He, B., Li, J., and Bao, Q. Impact of North Atlantic SST and Tibetan Plateau forcing on seasonal transition of springtime South Asian monsoon circulation. Clim. Dyn., 56(1), 559-579, 2021.

Zhang, M., Chen, Y., Shen, Y., and Li, B. Tracking climate change in Central Asia through temperature and precipitation extremes. J. Geogr Sci., 29(1), 3-28, 2019.

Zhang, S., Naik, V., Paynter, D., Tilmes, S., and John, J. Assessing GFDL-ESM4. 1 climate responses to a stratospheric aerosol injection strategy intended to avoid overshoot 2.0 C warming. Geophys. Res. Lett., 51(23), e2024GL113532, 2024a.

https://doi.org/10.5194/egusphere-2026-3008
Preprint. Discussion started: 2 July 2026

Zhang, W., Liu, L., Wu, H., Wang, L., Li, X., and Cheng, L. Increasing risks of compound heatwave and extreme precipitation events over the Tibetan plateau. J. Hydrol., 133983, 2025.

Zhang, X., Chen, C., and Zhao, W. Remote Insolation Forcing of Orbital-Scale South Asian Summer Monsoon Variability. Geophys. Res. Lett., 50(18), e2023GL105003, 2023.

Zhang, Y., MacMartin, D. G., Visioni, D., Bednarz, E. M., and Kravitz, B. Hemispherically symmetric strategies for stratospheric aerosol injection. Earth Syst. Dyn., 15(2), 191-213, 2024b.

Zhong, R., He, Y., and Chen, X. Responses of the hydrological regime to variations in meteorological factors under climate change of the Tibetan plateau. Atmos. Res., 214, 296-310, 2018.

Zhu, C., Ullah, W., Wang, G., Lu, J., Li, S., Feng, A., Hagan, D. F. T., Jiang, T., and Su, B. Diagnosing potential impacts of Tibetan Plateau spring soil moisture anomalies on summer precipitation and floods in the Yangtze River basin. J. Geophys. Res.: Atmos., 128(8), e2022JD037671, 2023.

Zhu, L., Ju, J., Qiao, B., Liu, C., Wang, J., Yang, R., Ma, Q., Guo, L., and Pang, S. Physical and biogeochemical responses of Tibetan Plateau lakes to climate change. Nat. Rev. Earth Environ., 1-15, 2025.

Zhu, Y., Yang, P., Xia, J., Huang, H., Chen, Y., Li, Z., Sun, K., Song, J., Shi, X., and Lu, X. Drought propagation and its driving forces in central Asia under climate change. J. Hydrol., 636, 131260, 2024.

Zou, S., Abuduwaili, J., Duan, W., Ding, J., De Maeyer, P., Van De Voorde, T., and Ma, L. Attribution of changes in the trend and temporal non-uniformity of extreme precipitation events in Central Asia. Sci. Rep., 11(1), 15032, 2021.

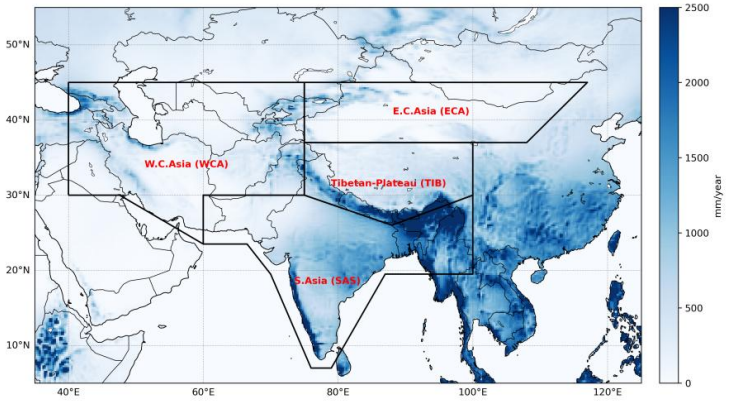

https://doi.org/10.5194/egusphere-2026-3008
Preprint. Discussion started: 2 July 2026

Figure 1. Spatial distribution of annually precipitation (2000–2024) from ERA5 reanalysis data over Asia. The sub-regions include Western Central Asia, Eastern Central Asia, Tibetan Plateau, and South Asia are outlined following the IPCC reference regions for Asia. (Iturbide et al., 2020).

https://doi.org/10.5194/egusphere-2026-3008
Preprint. Discussion started: 2 July 2026

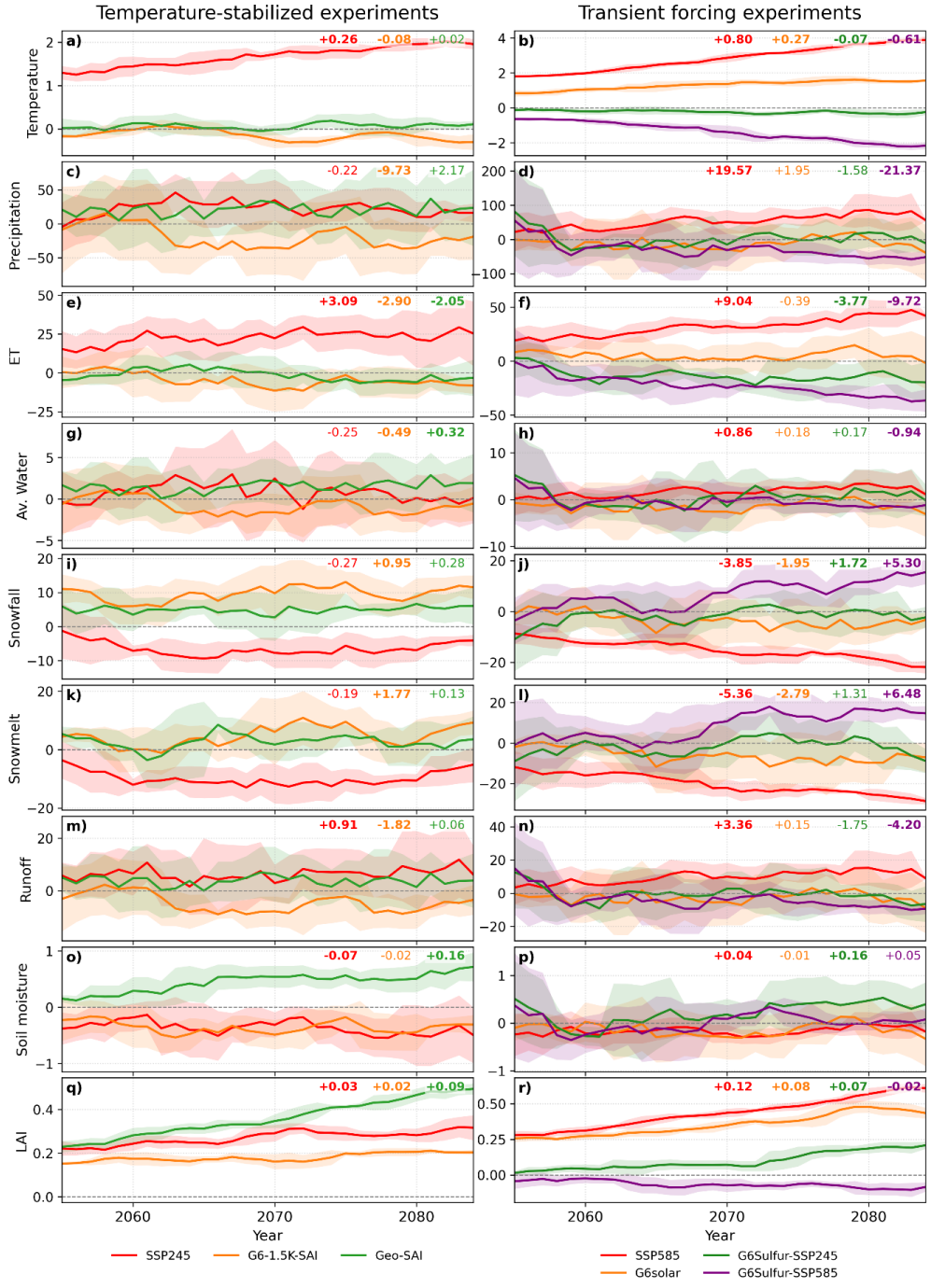

Figure 2. Annual mean anomalies of temperature, precipitation, ET, AW, snowfall, snowmelt, runoff, soil moisture, and LAI for 2055–2084 relative to the 2015–2034 mean, under temperature-stabilized experiments

https://doi.org/10.5194/egusphere-2026-3008
Preprint. Discussion started: 2 July 2026

(left column) and transient forcing experiments (right column). Colored lines show the time series for each scenario, and the colored numbers in the upper-right corner of each panel indicate the linear trend per decade for the corresponding scenario. Bold trend values denote trends that are statistically significant at the 95% confidence level. The horizontal dashed line marks zero anomaly.

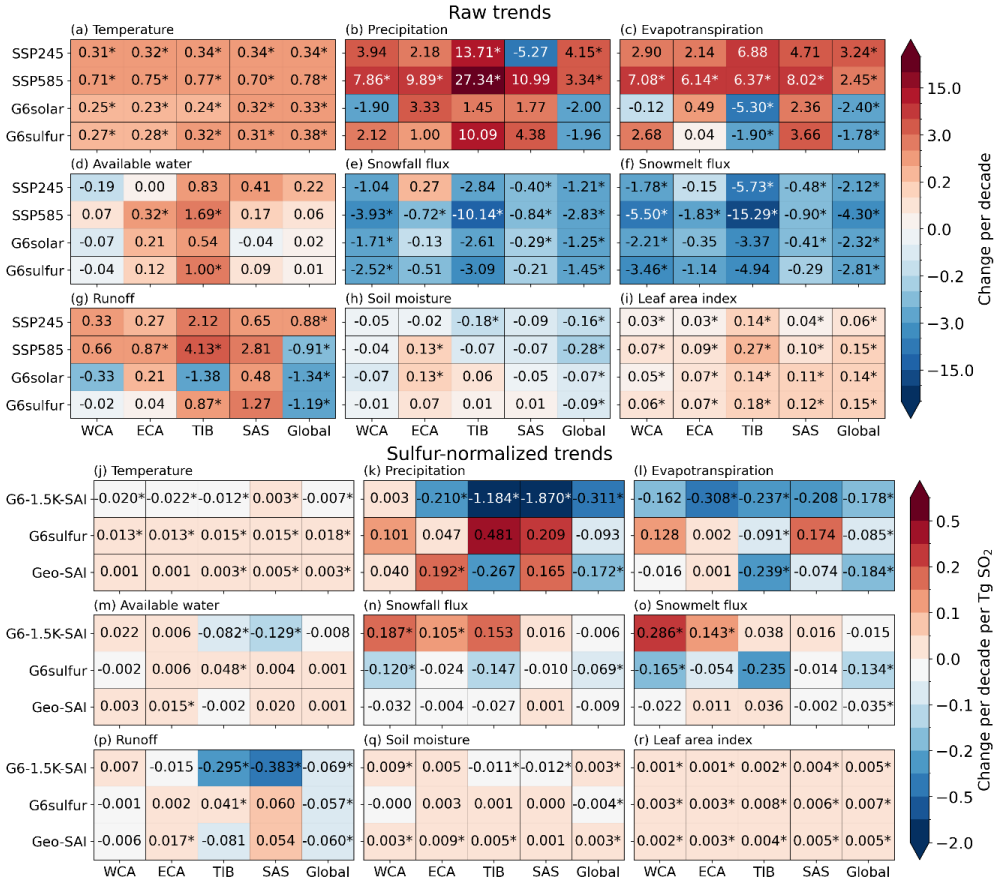

Figure 3. Future decadal trends of key hydro-climatic variables across WCA, ECA, TIB, SAS, and Global during 2035–2085. The upper panel (Raw trends; a–i) shows Sen's slope (change per decade) for SSP2-4.5, SSP5-8.5, G6Solar and G6Sulfur. The lower panel (Sulfur-normalized trends; j–r) shows Sen's slope for the SAI experiments (G6-1.5K-SAI, G6sulfur, and Geo-SAI), normalized by the mean sulfur injection rate (Tg SO_2 yr^{-1}) over 2055–2084 and expressed as change per decade per Tg SO_2. Panels (a–r) represent trends in temperature, precipitation, evapotranspiration, AW, snowfall flux, snowmelt flux, runoff, SM, and LAI, respectively. Colors indicate the magnitude and direction of Sen's slope, and asterisks denote statistically significant trends at the 95% confidence level based on the Mann–Kendall test.

https://doi.org/10.5194/egusphere-2026-3008
Preprint. Discussion started: 2 July 2026

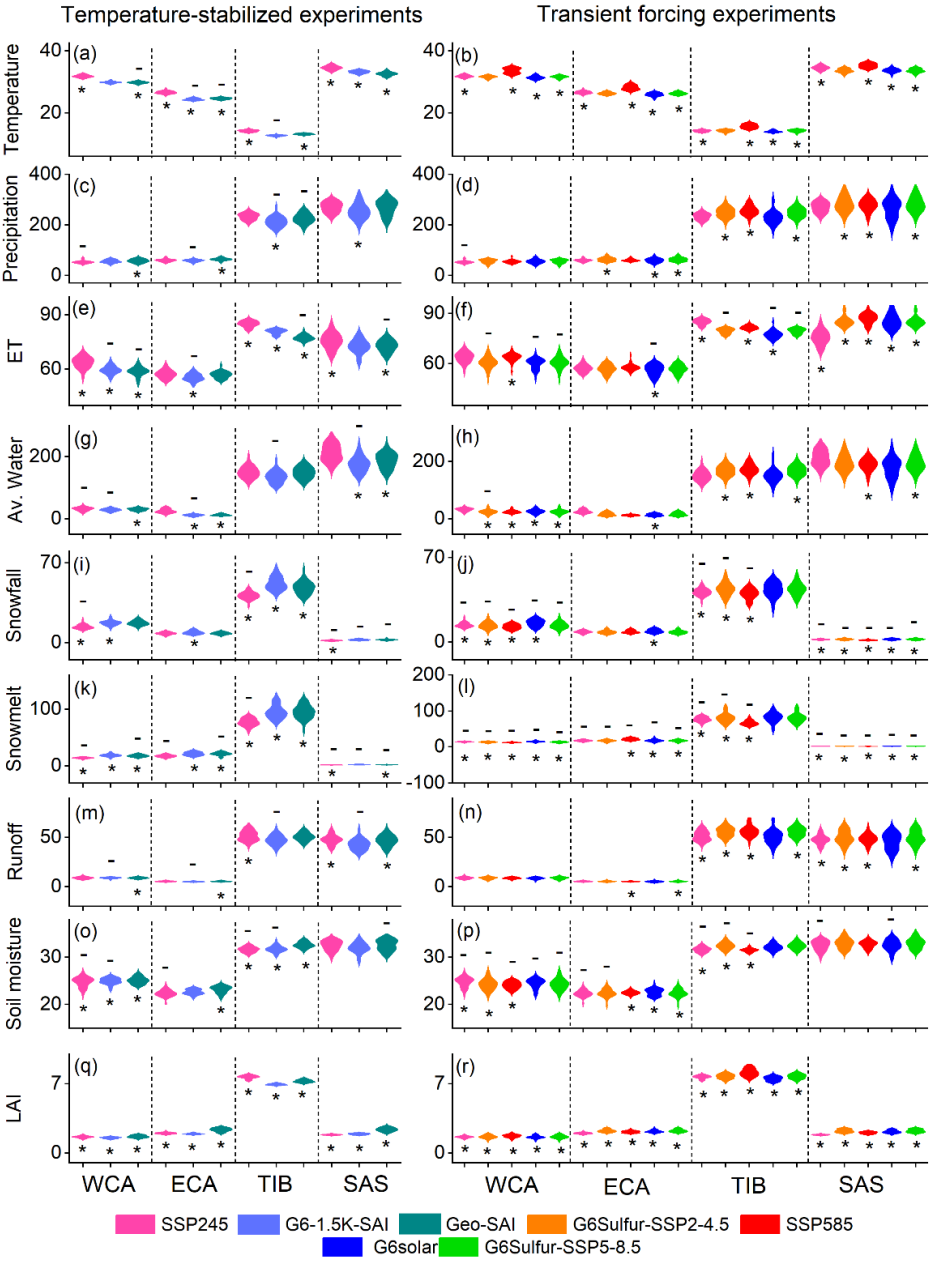

Figure 4. Regional distributions of annual peak changes in temperature (a, b), precipitation (c, d), ET (e, f), available water (g, h), snowfall (i, j), snowmelt (k, l), runoff (m, n), soil moisture (o, p), and LAI (q, r) across WCA, ECA, TIB, and SAS for temperature-stabilized (left column) and transient forcing (right column) experiments. The changes are calculated relative to 2015–2034 baselines, using SSP2-4.5 for SSP2-4.5, G6-1.5K-SAI, and SSP2-4.5-G6sulfur, and SSP5-8.5 for SSP5-8.5, G6solar, SSP5-8.5-G6sulfur, and Geo-SAI.

https://doi.org/10.5194/egusphere-2026-3008
Preprint. Discussion started: 2 July 2026

Negative values indicate decreases relative to the baseline, while positive values indicate increases. Asterisks denote changes significant at the 95% confidence level.

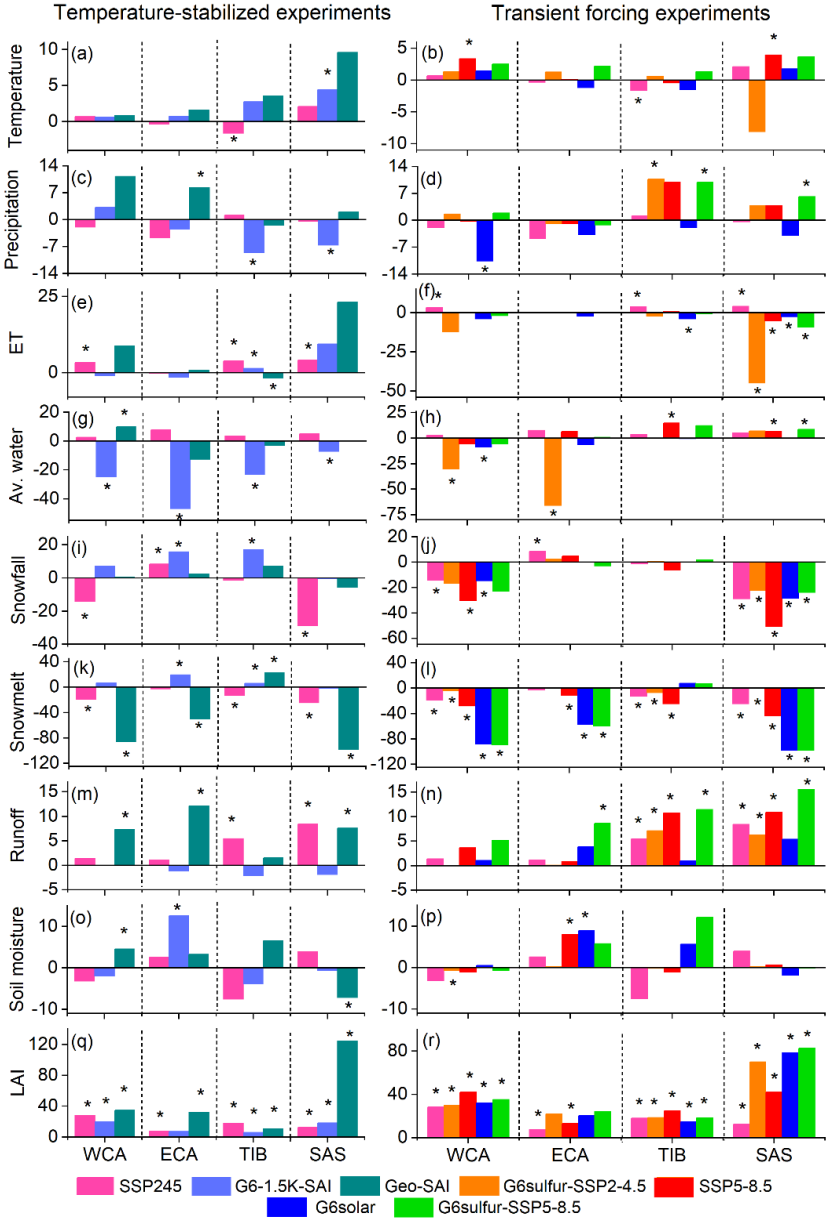

Figure 5. Percent change in the amplitude in temperature (a, b), precipitation (c, d), ET (e, f), available water (g, h), snowfall (i, j), snowmelt (k, l), runoff (m, n), soil moisture (o, p), and LAI (q, r) during 2055–2084 relative to present-day conditions (2015–2034) across WCA, ECA, TIB, and SAS for temperature-stabilized (left column) and transient forcing (right column) experiments. Changes are computed relative to scenario-specific baselines, using SSP2-4.5 for SSP2-4.5, G6-1.5K-SAI, and SSP2-4.5-G6sulfur, and SSP5-8.5 for

https://doi.org/10.5194/egusphere-2026-3008
Preprint. Discussion started: 2 July 2026

SSP5-8.5, G6solar, SSP5-8.5-G6sulfur, and Geo-SAI. Positive (negative) values indicate increases (decreases), and asterisks denote changes significant at the 95% confidence level based on a two-sided Welch's *t* test applied to ensemble distributions.

https://doi.org/10.5194/egusphere-2026-3008
Preprint. Discussion started: 2 July 2026

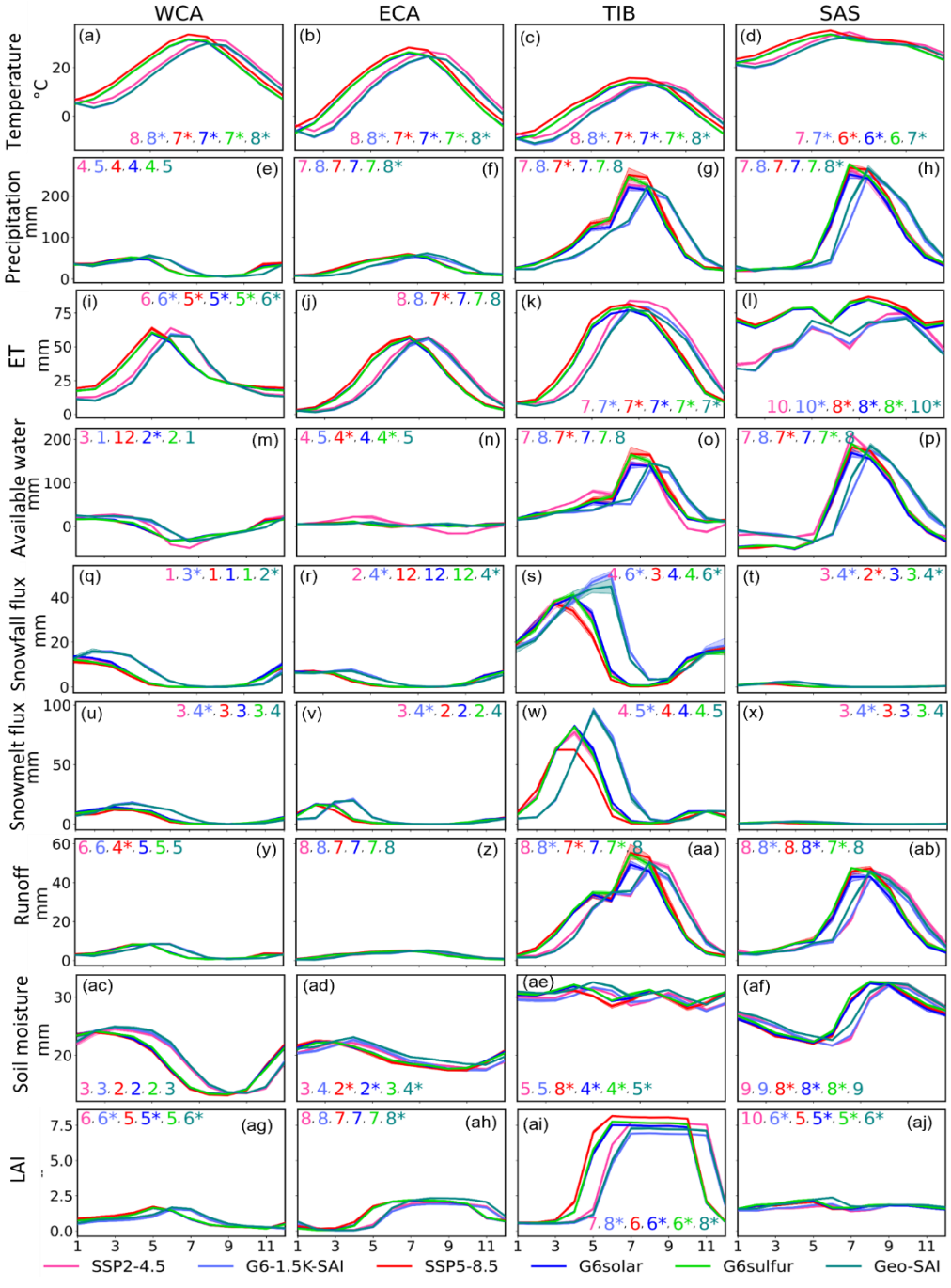

Figure 6. Seasonal cycles of key hydroclimatic variables over 2055–2084 for WCA, ECA, TIB, and SAS. Rows (top to bottom) show (a-d) temperature, (e-h) precipitation, (i-l) ET, (m-p) available water, (q-t) snowfall flux, (u-x) snowmelt flux, (y-ab) runoff, (ac-af) soil moisture, and (ag-aj) LAI. Colored curves

https://doi.org/10.5194/egusphere-2026-3008
Preprint. Discussion started: 2 July 2026

indicate the ensemble mean for each scenario (SSP2-4.5, G6-1.5K-SAI, G6sulfur-SSP2-4.5, SSP5-8.5, G6solar, G6sulfur- SSP5-8.5, Geo-SAI). Numbers shown at the top of each subplot indicate the mean peak month of the annual cycle for each scenario, and an asterisk denotes that the peak is statistically significant at the 95% confidence level.

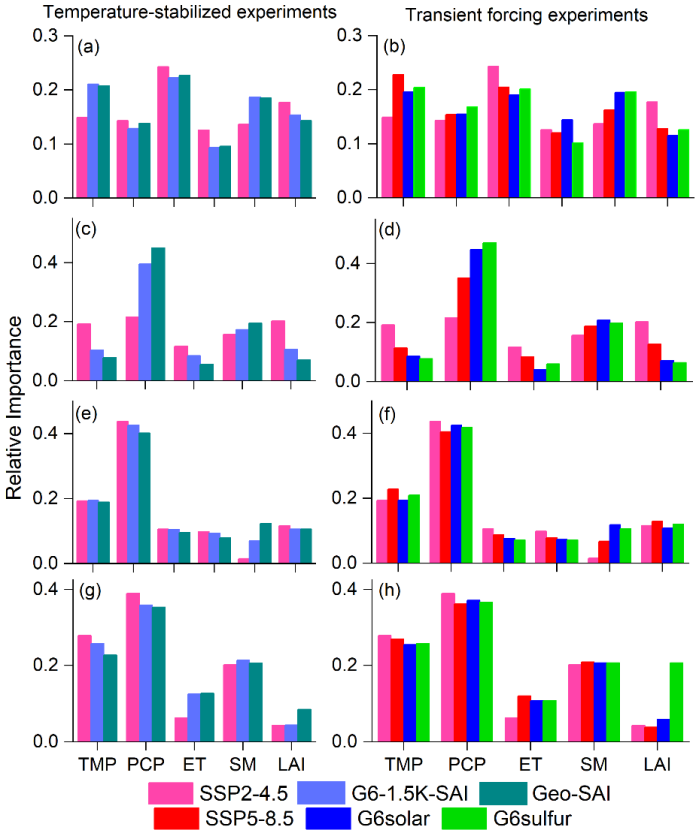

Figure 7. Relative importance of hydroclimatic predictors based on the LMG metric (Lindeman, Merenda, and Gold, 1980) for available water across (a, b) WCA, (c, d) ECA, (e, f) TIB, and (g, h) SAS. Panels are grouped into temperature-stabilized experiments (left column; SSP2-4.5, G6-1.5K-SAI, and Geo-SAI) and transient forcing experiments (right column; SSP2-4.5, SSP5-8.5, G6solar, and G6sulfur). Predictors include temperature (TMP), precipitation (PCP), ET, soil moisture (SM), and LAI. Bars represent the relative contribution of each predictor to the total explained variance of available water, and contributions within each panel sum to unity.

https://doi.org/10.5194/egusphere-2026-3008
Preprint. Discussion started: 2 July 2026

Table 1. Percent changes (%) in regional mean annual temperature (TMP), precipitation (PCP), ET, Av. water, snowfall, snowmelt, runoff, soil moisture, and LAI for 2055–2084 relative to 2015–2034 over WCA, ECA, TIB, and SAS under SSP245, SSP585, G6-1.5K-SAI, G6solar, G6sulfur-SSP245, G6sulfur-SSP585, and Geo-SAI. Values for SSP245, G6-1.5K-SAI, and G6sulfur-SSP245 are referenced to the SSP245 baseline, while values for SSP585, G6solar, G6sulfur-SSP585, and Geo-SAI are referenced to the SSP585 baseline, both for 2015–2034. Bold values denote statistically significant changes at the 95% level.

Region	Scenario	TMP	PCP	ET	Av. water	Snowfall	Snowmelt	Runoff	Soil moisture	LAI
WCA	SSP245	**9.8**	-0.16	**4.4**	< -100	**-12.9**	**-14.5**	1.06	**-2.7**	**24.9**
	SSP585	**15.9**	**6.1**	**6.4**	-8.9	**-26.1**	**-28.1**	4.0	**-2.2**	**46.1**
	G6-1.5K-SAI	**-1.5**	0.21	-1.57	< -100	**18.1**	**8.6**	-2.2	**-1.4**	**18.2**
	Geo-SAI	**-3.4**	4.09	**-10.4**	**< -100**	**12.8**	**7.0**	2.8	**2.0**	**43.8**
	G6solar	**5.1**	-0.52	0.49	-9.2	**-9.2**	**-8.4**	-0.98	**-1.7**	**35.7**
	G6sulfur-SSP245	**8.5**	-4.0	**10.1**	**< -100**	**-17.3**	**-18.5**	**-8.6**	**-4.3**	**28.2**
	G6sulfur-SSP585	**5.7**	-0.67	1.15	-16.6	**-19.0**	**-18.1**	-2.6	**-1.5**	**37.0**
ECA	SSP245	**18.2**	**6.9**	**4.1**	27.0	1.66	-0.88	2.67	-0.87	**15.0**
	SSP585	**31.0**	**12.3**	**8.3**	**45.1**	**-7.4**	**-12.4**	**11.4**	**1.95**	**33.8**
	G6-1.5K-SAI	**-6.1**	-1.6	**-5.7**	27.6	**21.4**	**8.3**	**-6.7**	-0.92	**6.2**
	Geo-SAI	**-4.9**	**4.4**	-1.59	**53.0**	**11.8**	**8.4**	**4.7**	**5.5**	**34.1**
	G6solar	**10**	**4.2**	0.50	**34.8**	0.26	-0.66	4.1	**2.5**	**27.9**
	G6sulfur-SSP245	**12.5**	**4.7**	-0.71	**46.4**	-4.82	**-7.07**	-2.40	-0.42	**25.5**
	G6sulfur-SSP585	**10.2**	**4.2**	0.96	**31.0**	-5.6	**-6.7**	3.01	**2.2**	**29.3**
TIB	SSP245	**>100**	**5.2**	**7.4**	**6.8**	**-8.1**	**-10.2**	**3.2**	**-2.6**	**22.2**
	SSP585	**>100**	**11.4**	**6.5**	**15.1**	**-19.5**	**-20.6**	**7.8**	-0.63	**32.5**
	G6-1.5K-SAI	**-10.3**	**-2.9**	**-2.2**	-1.99	**18.4**	2.5	**-6.1**	**-3.0**	**7.7**
	Geo-SAI	-1.8	-0.98	**-5.7**	2.9	**10.0**	-0.40	-1.3	**1.9**	**13.6**
	G6solar	**66.8**	-0.86	**-2.5**	0.41	**-8.08**	**-6.4**	-2.1	0.52	**18.7**
	G6sulfur-SSP245	**>100**	**8.1**	0.33	**16.0**	**-10.8**	**-11.0**	**3.9**	-0.39	**21.8**
	G6sulfur-SSP585	**77.4**	**6.0**	-0.06	**10.8**	**-12.4**	**-10.9**	**4.6**	**1.03**	**22.2**
SAS	SSP245	**5.9**	2.7	**5.0**	3.9	**-28.4**	**-29.8**	**8.4**	-0.17	**18.5**
	SSP585	**10**	**5.3**	**5.2**	5.4	**-48.7**	**-51.3**	**8.7**	-0.67	**28.6**
	G6-1.5K-SAI	**1.07**	-3.5	1.1	-10.7	7.9	2.1	-2.4	-0.9	**21.5**
	Geo-SAI	0.20	3.6	**-22.2**	**64.8**	1.5	-5.1	5.1	**1.1**	**38.0**
	G6solar	**4.7**	-1.4	**2.0**	-12.5	**-24.6**	**-23.6**	0.03	-1.0	**30.5**
	G6sulfur-SSP245	**5.2**	**7.1**	**38.3**	**-28.4**	**-28.0**	**-28.6**	**13.6**	**2.0**	**33.3**
	G6sulfur-SSP585	**4.3**	**6.1**	**3.7**	13.3	**-25.8**	**-25.1**	**9.7**	0.98	**35.3**